Lecithin:Retinol Acyl Transferase (LRAT) induces the formation of lipid droplets

Martijn R. Molenaar[§], Tsjerk A. Wassenaar[‡], Kamlesh K. Yadav[#], Alexandre Toulmay[#], Muriel C. Mari[&], Lucie Caillon[£], Aymeric Chorlay[£], Maya W. Haaker[§], Richard W. Wubbolts[§], Martin Houweling[§], A. Bas Vaandrager[§], Fulvio Reggiori[&], Abdou Rachid Thiam[£], William A. Prinz[#], J. Bernd Helms[§]*

[§] Department of Biochemistry and Cell Biology, Faculty of Veterinary Medicine, Utrecht University, 3584 CM, Utrecht, The Netherlands
[‡] Groningen Biomolecular Sciences and Biotechnology Institute and Zernike Institute for Advanced Materials, University of Groningen, Nijenborgh 7, 9747 AG Groningen, The Netherlands
[#] National Institute of Diabetes and Digestive and Kidney Diseases, NIH, Bethesda, MD 20892, USA
[&] Department of Cell Biology, University of Groningen, University Medical Center Groningen, Groningen, Netherlands
[£] Laboratoire de Physique Statistique, Ecole Normale Supérieure, PSL Research University, Sorbonne Université, UPMC Université Paris 06, Université Paris Diderot, CNRS, Paris, France.

* To whom correspondence should be addressed: J.B.H (J.B.Helms@uu.nl)

Abstract

Lipid droplets are unique and nearly ubiquitous organelles that store neutral lipids in a hydrophobic core, surrounded by a monolayer of phospholipids. The primary neutral lipids are triacylglycerols and steryl esters. It is not known whether other classes of neutral lipids can form lipid droplets by themselves. Here we show that production of retinyl esters by lecithin:retinol acyl transferase (LRAT) in yeast cells, incapable of producing triacylglycerols and steryl esters, causes the formation of lipid droplets. By electron microscopy, these lipid droplets are morphologically indistinguishable from those in wild-type cells. *In silico* and *in vitro* experiments confirmed the propensity of retinyl esters to segregate from membranes and to form lipid droplets. The hydrophobic N-terminus of LRAT displays preferential interactions with retinyl esters in membranes and promotes the formation of large retinyl ester-containing lipid droplets in mammalian cells. Our combined data indicate that the molecular design of LRAT is optimally suited to allow the formation of characteristic large lipid droplets in retinyl ester-storing cells.

Keywords

LRAT; vitamin A; retinol; retinyl ester; retinoids; lipid droplets; lipid droplet size; nucleation; lipid:protein interaction; hepatic stellate cells; liver

Introduction

Lipid droplets (LDs) form a ubiquitous class of organelles, best known for their role as storage of neutral lipids for a multitude of functions such as creating an energy reservoir, a source for building blocks, protection against lipotoxicity, a role in cell cycle, and storage of signaling lipids (Hashemi and Goodman, 2015; Pol et al., 2014; Thiam and Beller, 2017; Walther and Farese, 2012). However, LDs also play important roles in lipid metabolism and homeostasis. Dysfunction of LD synthesis has been linked to a range of diseases. The physiological role of LDs thus appears significantly larger than considered previously (Krahmer et al., 2013; Welte, 2015).
LDs have a unique organellar architecture with a lipid monolayer surrounding a hydrophobic core that consists of neutral lipids. A number of specific proteins associate with LDs regulating organelle and lipid dynamics. Recent advances have started to shed light on the mechanism of LD biogenesis. In the most prevalent view, LD formation is primarily driven by triacylglycerol (TAG) synthesis at the endoplasmic reticulum (ER). TAG accumulates at the interphase of the ER bilayer, until a critical demixing concentration is reached and phase separation occurs, leading to lens formation and membrane deformation (Thiam and Forêt, 2016; Walther et al., 2017). During this process of nucleation, neutral lipids coalesce to form lenses between the two leaflets of the membrane bilayer. Indeed, lenses of about 50nm have been observed in the ER upon induction of LD formation in yeast (Choudhary et al., 2015). As neutral lipid synthesis continues, nascent LDs may bud from the endoplasmic reticulum. Although this process may not require proteins other than TAG synthesizing enzymes such as DGAT 1/2 and ACSL3 (Kassan et al., 2013; Pol et al., 2014; Thiam and Forêt, 2016; Walther et al., 2017), several proteins and lipids have been identified in the regulation of LD number and size as well as LD dynamics.

The abundant presence of large LDs is a hallmark of hepatic stellate cells (HSCs) in normal liver. HSCs are specialized in the storage of retinol (vitamin A) as retinyl esters, giving the LDs their characteristic autofluorescent properties. After liver injury, the fine structure of HSCs changes considerably. They lose their characteristic LDs and transdifferentiate into myofibroblasts, in preparation to secrete collagen (Blaner et al., 2009; Friedman, 2008). Lipidomic analysis revealed complex dynamics of disappearance of different classes of neutral lipids during HSC activation (Testerink et al., 2012). Recent research shows the presence of two different types of LDs, so-called preexisting "original" LDs with relatively slow turnover and rapidly "recycling" LDs that transiently appear during activation of HSCs (Ajat et al., 2017; Molenaar et al., 2017; Tuohetahuntila et al., 2016). Whereas synthesis and breakdown of TAGs in rapidly recycling LDs is mediated by DGAT1 and ATGL (Tuohetahuntila et al., 2016), less is known about the turnover of preexisting LDs. Lysosomes play an important role in the degradation of these LDs (Tuohetahuntila et al., 2017) and this is likely to be related to the observed importance of the autophagic pathway in HSC activation (Hernandez-Gea and Friedman, 2011; Thoen et al., 2011).

Surprisingly, inhibition of DGAT1 does not affect the dynamics of the preexisting LDs nor does it affect the synthesis of retinyl esters in isolated primary HSCs (Ajat et al., 2017;

67   Tuohetahuntila et al., 2016). However, HSCs contain a specialized enzyme called
68   lecithin:retinol acyltransferase (LRAT) that catalyzes a trans-esterification reaction
69   between the *sn-1* position of phosphatidylcholine (PC) and all-*trans*-retinol to form
70   all-*trans*-retinyl ester (Fig. 1A,B) (Golczak et al., 2012; Ruiz and Bok, 2010). As LRAT is
71   the main contributor to retinyl ester storage in the liver (Liu and Gudas, 2005; O'Byrne et
72   al., 2005), we investigated the possibility that LRAT-mediated retinyl ester synthesis
73   drives the generation of the relatively large, retinyl ester-containing LDs in quiescent
74   HSCs.
75

Results

LRAT expression generates UV-positive lipid droplets

Primary and quiescent HSCs spontaneously transdifferentiate into activated HSCs (myofibroblasts) *ex vivo* upon isolation and subsequent culture, resulting in LD disappearance. Quiescent and activated HSCs can be identified based on their high expression of desmin, whereas these two HSC populations can be distinguished from each other by an increased alpha smooth muscle actin (α-SMA) expression in activated HSCs (Blaner et al., 2009; Friedman, 2008) (Fig. 1C,D). In addition, LRAT expression decreases (Blaner et al., 2009; Kluwe et al., 2011) (Fig. 1E). We previously presented evidence for neutral lipid dynamics during HSC activation that is consistent with the existence of two different pools of LDs (Molenaar et al., 2017; Tuohetahuntila et al., 2017). To visualize these two different pools, we made use of the autofluorescent properties of retinyl esters in preexisting "original" LDs that are a hallmark of quiescent HSCs (Ajat et al., 2017; Friedman, 2008). After fixation of freshly isolated HSCs, retinyl esters (UV autofluorescence) and LDs (LD540) were imaged by confocal microscopy. We observed two distinct populations of LDs: large UV^+LD540^+ structures containing high amounts of REs and UV^-LD540^+ structures - depleted from REs - with smaller diameters (Fig. 1F). These observations are also in good agreement with our recent findings that LDs in $LRAT^{-/-}$ HSCs were significantly smaller as compared to LDs from wild-type cells (Ajat et al., 2017). Together, these data suggest a role for LRAT in the formation of distinct vitamin A-containing LDs that are a hallmark of hepatic stellate cells (HSCs).

To understand the role of LRAT in LD biology, we stably transfected CHO-k1 cells with a plasmid carrying LRAT-GFP. Lipidomic analysis of CHO cells expressing LRAT showed that retinyl ester synthesis was observed only after addition of retinol (ROH) as substrate to the medium (Fig. 1G (UV^+LDs) and Suppl. Fig. 1A) and revealed the presence of predominantly saturated (16:0 and 18:0) and mono-unsaturated (18:1) fatty acids (Suppl. Fig. 1A). This composition reflects the catalytic activity of LRAT, using fatty acids at the *sn-1* moiety of PC for esterification (Golczak et al., 2012; MacDonald and Ong, 1988). CHO cells do not contain detectable amounts of enzymatic activity of LRAT (Suppl. Fig. 1B) and in the absence of LRAT they can synthesize retinyl esters using a different mechanism involving DGAT1 (Ajat et al., 2017; Orland et al., 2005). This reaction occurs with much lower efficiency and results in a different species profile of retinyl esters (Suppl. Fig. 1C). Inhibition of DGAT1 activity in CHO-k1 cells expressing LRAT-GFP showed no inhibition of retinyl ester synthesis, which confirms that LRAT is the primary retinyl ester synthesizing enzyme (Suppl. Fig. 1D). Both CHO-k1 cells expressing GFP or LRAT-GFP showed increased LD540 fluorescence after incubation with oleic acid (OA). However, only LRAT-GFP expressing cells showed an increase in LDs after incubation with ROH, confirming the ability of LRAT to esterify ROH (Fig. 1G). Furthermore, these LDs exhibited UV-autofluorescence and were larger in diameter as compared to OA-stimulated LDs, which in turn were not autofluorescent (Fig. 1H). Similar results were obtained after transfection of human HSC-derived cell line LX-2 with LRAT (Suppl. Fig. 2). To exclude the possibility that the observed large UV^+LDs were in fact clusters of small LDs that could not be distinguished due to the limited resolution of conventional confocal microscopy, we also imaged both conditions

122   by super resolution microscopy (3D structured illumination microscopy, 3D-SIM). Using
123   SIM, we observed both small and large sized LDs in LRAT-dependent LD-synthesis and
124   with a clustered appearance (Fig. 1I). In the presence of OA, the LDs displayed a more
125   homogeneous size-distribution of relative small LDs and a 'dispersed' localization
126   through the cell (Fig. 1I, Suppl. Video 1-2).
127

LRAT-mediated LD formation is independent of TAG synthesis.
129   TAG synthesis is a driving force in LD biogenesis. The last step in TAG synthesis is
130   performed by DGAT1 or DGAT2, enzymes that transfer activated fatty acids to
131   diacylglycerol. Fatty acid activation is performed by acyl-CoA synthetases and their
132   knockdown or pharmaceutical inhibition after OA-stimulation led to a decreased number
133   of (pre-)LDs (Kassan et al., 2013). Acyl-CoA is, however, not involved in the
134   transesterification reaction of a fatty acid from PC to ROH by LRAT to generate retinyl
135   esters. To determine whether LRAT requires TAG synthesis for retinyl ester synthesis and
136   formation of RE-containing LDs, we pre-incubated LRAT-GFP expressing cells under
137   low serum conditions overnight and subsequently incubated the cells in the presence of
138   triacsin C, a drug that inhibits acyl-CoA synthesizing activities (Igal et al., 1997). In the
139   presence of triacsin C, the number of LDs was strongly reduced, both in the presence and
140   absence of OA (Fig. 2A). In the presence of ROH, however, formation of large LDs was
141   still observed. These results confirm that LRAT does not depend on the presence of
142   acyl-CoA and supports the possibility that LD-formation via LRAT has a distinct
143   mechanism that is independent of TAG (DGAT/ACSL-mediated) LD formation.
144

145   Some LDs could still be observed in cells treated with triacsin C and therefore we could
146   not exclude the possibility that, rather than TAG synthesis, TAG-filled LDs are required
147   for RE-containing LD formation. Therefore, we made use of another model system, a
148   *Saccharomyces cerevisiae* mutant strain that lacks the four enzymes responsible for the
149   last steps in triglyceride - Lro1 and Dga1 - and steryl ester (SE) - Are1 and Are2 -
150   synthesis. This mutant strain is viable, but does not contain LDs (Sandager et al., 2002).
151   After introduction of human LRAT into *lro1Δ dga1Δ are1Δ are2Δ* cells (hereafter 4Δ
152   cells), LRAT-GFP co-localizes with Sec63-mCherry, an ER marker in yeast (Suppl. Fig.
153   3A). The resulting LRAT expressing yeast cells (4Δ LRAT) were able to synthesize REs
154   after the addition of ROH (Fig. 2B). In contrast to mammalian cells, the predominant
155   RE-species was retinyl palmitoleate, RE(16:1). This is in line with the reported fatty acid
156   composition of PC in yeast, which is capable of producing only monounsaturated fatty
157   acids, and contains predominantly PC(32:2) and PC(34:2) (Boumann et al., 2006). In the
158   absence of either LRAT or ROH, both 4Δ and wild-type (*wt*) yeast cells did not
159   synthesize REs. These results also demonstrate the absence of an endogenous RE
160   synthase activity in yeast by acyl-CoA retinol acyltransferase (ARAT) activity e.g. Dga1
161   (Fig. 2B). Thus, RE synthesis in yeast depends on LRAT expression. As anticipated, 4Δ
162   LRAT yeast cells were devoid of LD structures in the absence of exogenous ROH, as
163   evidenced by membrane localization of LD-marker Erg6 (Fig. 2C) and BODIPY (Suppl.
164   Fig. 3B). Upon addition of ROH to 4Δ LRAT yeast cells, we observed a clear presence of
165   autofluorescent LD-like structures and co-localization of these structures with the
166   LD-marker Erg6 (Fig. 2C, Suppl. Fig. 3C) and with BODIPY (Suppl. Fig. 3B). In the
167   absence of LRAT, 4Δ yeast cells could not generate LDs in the presence of ROH.

168   Electron microscopic examination of the LDs generated in 4Δ LRAT yeast cells revealed
169   the presence of *bona fide* LDs with a cytosolic orientation that were morphologically
170   indistinguishable from TAG/SE-filled LDs generated in wt yeast cells (Fig. 2D,E). These
171   results demonstrate that LRAT induces the formation of LDs in the absence of other LDs
172   or TAGs (Suppl. Fig. 4). To determine whether retinyl esters can partition into existing
173   LDs or exclusively form their own LDs, we determined the co-localization of RE positive
174   LDs (UV$^+$) with all LDs (Erg6$^+$) immediately after addition of ROH to *wt* yeast cells
175   expressing LRAT. These cells have TAG-filled LDs present before addition of ROH. As
176   shown in Fig. 2F, 2 min after addition of ROH, co-localization of Erg6$^+$ LDs with UV$^+$
177   LDs was observed. In addition, UV$^-$ LDs become UV$^+$ in the next 6 min, indicating that
178   REs are also transferred into existing LDs.
179
180   **Spontaneous nucleation and lens formation of retinyl esters in lipid bilayers**
181   The mechanism of LD formation by LRAT-mediated RE synthesis is not known. For
182   TAG-filled LDs it has been shown that TAGs have a limited solubility in biological
183   membranes. Above a critical demixing concentration (~3%), TAG molecules segregate to
184   form TAG lenses that appear as a first step in LD formation (Choudhary et al. 2015;
185   Khandelia et al., 2010; Thiam and Forêt, 2016). After this 'nucleation' process, the lenses
186   grow and can emerge from ER membranes during a 'budding' process. The formation of
187   lenses in TAG containing membranes has been demonstrated and studied in molecular
188   dynamics (MD) simulations (Ben M'barek et al., 2017; Khandelia et al., 2010). Here we
189   built upon that approach and used coarse-grain MD (CG-MD) simulations of
190   1-palmitoyl-2-oleoyl-sn-glycero-3-phosphocholine (POPC) membranes with different
191   amounts of trioleoylglycerol (TOG) and retinyl palmitate (RP) to assess the propensity of
192   lens formation in those systems. In setups containing only TOG, lens-formation was
193   consistently observed and always completed within 100 ns of simulation. In contrast,
194   setups with only RP took considerable longer to nucleate (Fig. 3A) and more often failed
195   to form lenses on the time scale used for the simulations (250 ns). Lenses formed by RP
196   were also typically less well defined, with more RP remaining dispersed throughout the
197   membrane. Mixtures of TOG and RP showed an intermediate efficiency of lens-formation
198   (Fig. 3A and B). These simulations imply that RP has a lower propensity to self-aggregate,
199   and hence has a higher nucleation barrier as compared to TOG.
200   Methods to directly measure the nucleation barrier (or 'critical nucleation volume') do
201   not exist, but in a setting with the same PL-composition, the monolayer surface tension
202   will be a driving force that affects nucleation (Ben M'barek et al., 2017; Deslandes et al.
203   2017; Thiam and Forêt, 2016). The deformation and budding of a LD monolayer is
204   controlled in part by the monolayer bending rigidity and surface tension – the monolayer
205   bending rigidity will tend to flatten a lens, thereby re-dispersing neutral lipid molecules in
206   the bilayer, while its surface tension will tend to make a lens spherical. However, at a
207   characteristic size, surface tension will essentially control the monolayer deformation.
208   This size will be larger for a lower monolayer surface tension: lower monolayer tensions
209   will likely result in larger 'critical nucleation volumes' or higher nucleation barriers (Ben
210   M'barek et al., 2017; Chorlay and Thiam, 2018; Deslandes et al., 2017; Thiam and Forêt,
211   2016). We measured the tension of artificial LD containing either RP or TOG and, in line
212   with our MD simulations, tensions were considerably lower in droplets made of RP as
213   compared to their TOG counterparts (Table 1). Moreover, droplets surrounded by DOPC

7

214 with maximum phospholipid packing showed the same trend. These measurements
215 suggest that RP droplets have higher nucleation barriers, in agreement with the results
216 obtained by CG-MD.
217 The efficiency of the subsequent budding process of RE-containing LDs can be studied
218 by determination of budding angles in droplet-embedded vesicles or droplet interface
219 bilayers (DIBs) containing neutral lipids (Ben M'barek et al., 2017; Chorlay and Thiam,
220 2018). By using the DIB system, we compared the budding angles of RP-containing lipid
221 phase with reported values of TAG-LDs (Fig. 3C,D). The budding angles of RP$^+$ droplets
222 with PC and PE monolayers did not differ from reported values of their TOG$^+$
223 counterparts (Fig. 3D); angles in the case of PA were only slightly higher. These data
224 suggest that RP forms spontaneously LDs as efficiently as TG. In PC tensionless
225 membranes, smaller RP-LD diameters would be thus expected, based on the budding
226 angles, but the delay in nucleation might introduce an increase in the droplet size. This is,
227 however, not observed in yeast cells (Fig. 2C). Thus, other factors must contribute to the
228 characteristic large size of retinyl ester-containing LDs.
229
230 **N-terminal sequence of LRAT affects lipid droplet morphology**
231 To study a role of LRAT in LD morphology, we considered the possibility that the
232 N-terminus of LRAT aids in the formation of LDs. The N-terminal domain of LRAT
233 (hereafter, LRAT-Nt AH) does not form a trans-membrane domain, despite its high
234 hydrophobicity (Moise et al., 2007). In addition, it was reported that this domain can
235 localize to LDs (Jiang and Napoli, 2012). We stably transfected CHO-k1 cells with a GFP
236 fusion construct of LRAT lacking the N-terminus (ΔNt-LRAT-GFP) and selected clones
237 with similar GFP fluorescence as compared to CHO-k1 cells stably transfected with
238 full-length LRAT-GFP (Fig. 1). LRAT-activity of both homogenates was analyzed *in vitro*
239 using HPLC-MS/MS by determination of RE(7:0) synthesis upon addition of exogenous
240 PC(7:0/7:0) (Fig. 4A, see Materials and Methods for details). As expected, both enzymes
241 displayed LRAT-activity with similar K_m-values for ROH, but reaction rates of
242 ΔNt-LRAT-GFP homogenates were somewhat lower (Fig. 4B). After overnight
243 incubation with ROH, we observed UV$^+$ LDs in both cell lines, but LDs appeared smaller
244 in size in ΔNt-LRAT-GFP expressing cells (Fig. 4C,D). These data show that the
245 N-terminus is not required *per se* for LD generation, but may have an effect on LD
246 morphology. To rule out the possibility that the reduced LD size in the presence of
247 ΔNt-LRAT-GFP is caused by the reduced activity of this LRAT mutant (Fig. 4B), we
248 developed a single-cell imaging analysis pipeline. To this end, we determined cell size,
249 LD-number per cell and mean LD size per cell by image analysis (see Materials &
250 Methods for details). Total LD volume (representative for total neutral lipid content) was
251 calculated from these parameters. Using this approach, we were able to select ("gate")
252 cells with similar total LD volume and thus neutral lipid content per cell (Fig. 4E). We
253 then compared the log-ratios of LD number *vs.* LD volume per cell of both cell lines
254 incubated with OA or ROH (Fig. 4F). As expected, no difference was observed when
255 both cell lines were incubated with OA (Fig. 4F, left panel). In contrast, LDs generated in
256 the presence of ROH were smaller in size and larger in number in cells expressing
257 ΔNt-LRAT-GFP as compared to LDs from cells expressing the full-length protein, as
258 reflected by decreased log-ratios (Fig. 4F, right panel). This difference in LD size:number
259 distribution could also be observed in ungated cells; expressing LD-number as function of

260 the total LD volume per cell showed that regression of all datapoints of LRAT lacking its
261 N-terminus results in a steeper slope as compared to full-length LRAT, indicating more
262 LDs per amount of total neutral lipid (Fig. 4G). Taken together, these results show that
263 the LRAT-Nt has the ability to affect the size:number distribution of retinyl
264 ester-containing LDs in mammalian cells.
265
266 **N-terminus of LRAT exhibits affinity for retinyl esters *in silico***
267 The N-terminus of LRAT is predicted to have an alpha-helical structure without hairpin
268 topology, which is flanked by amino acids without a clear secondary structure (Suppl. Fig.
269 5). HeliQuest analysis (Gautier et al., 2008) showed a clear separation between
270 hydrophobic and polar residues on both sides of the helix, in line with an amphipathic
271 topology (Fig. 5A, upper panel). However, in comparison with canonical amphipathic
272 helices involved in membrane recognition (ALPS motifs) (Bigay et al., 2005), the
273 fraction of hydrophobic over polar residues was considerably higher in the LRAT
274 N-terminal alpha-helix. This is exemplified by comparison of this projection with CCT-α
275 P2, a recently characterized amphipathic domain with LD-affinity (Prévost et al., 2018)
276 that contains an ALPS-like architecture (Fig. 5A, bottom panel). The helical wheel
277 projection of the CCT-α P2 AH revealed a smaller fraction of hydrophobic residues as
278 compared to the LRAT-Nt AH. Membrane-binding of CCT-α P2 is proportional to the
279 amount of lipid packing defects (Prévost et al., 2018). We compared the
280 membrane-binding characteristics of LRAT-Nt with CCT-α P2 by CG-MD using the
281 DAFT-approach (ensemble of 30 simulations per combination of peptide and model
282 membrane) (Wassenaar et al., 2015a). One model membrane consisted of POPC and the
283 other one contained POPC and dioleylglycerol (DOG), a lipid that induces packing
284 defects (Vamparys et al., 2013). We subsequently compared membrane binding of both
285 LRAT-Nt and CCT-α P2. The binding half-time of CCT-α P2 to POPC membranes was
286 150 ns (Fig. 5B, bottom panel) and in the presence of DOG, this binding was accelerated
287 (50 nsec) (Fig. 5B, bottom panel), confirming the role of packing defects in membrane
288 binding (Prévost et al., 2018). For LRAT-Nt, however, we did not observe a difference in
289 the kinetics of membrane binding between the two model systems (Fig. 5B, top panel;
290 median of about 60 nsec). Interestingly, the results also showed that LRAT-Nt AH docked
291 deeper into the bilayer than the CCT-α P2 AH (Fig. 5C), suggesting that LRAT-Nt has the
292 potential to directly interact with neutral lipids, whereas CCT-α P2 AH binds only to
293 phospholipids.
294
295 To investigate a potential interaction of the N-terminal peptide with neutral lipids, we
296 extended the MD setup to a series of POPC membranes containing 10% neutral lipids in
297 different ratios RP:TOG, and in the presence of LRAT-Nt. The simulations showed that
298 LRAT-Nt typically co-localized with neutral lipids (Fig. 6A). Inspection of the
299 localization of LRAT-Nt with respect to the membrane profile (Fig. 6B; Suppl. Fig. 6A)
300 confirmed that the peptide is docked deep into the membrane. Surprisingly, LRAT-Nt is
301 docked deeper into the membrane when the neutral lipids consist predominantly of RP as
302 opposed to TOG (Fig. 6B). This is only partly explained by the thicker membrane
303 resulting from the more complete lens formation at higher TOG ratios.
304 Initial inspection of the localization of TOGs and RPs within the lens revealed an
305 asymmetric distribution of the neutral lipid mixture with RPs in closer proximity to the

9

306   LRAT-Nt peptide (Suppl. Fig. 6B). Assessment of the interaction energies between the
307   LRAT-Nt helix and both RP and TOG confirmed that the helix has stronger interactions
308   with RP than it has with TOG (Fig. 6C). This specific affinity of LRAT-Nt for REs could
309   affect lens and/or LD formation by REs, for example by facilitating the formation of RP
310   containing lenses by decreasing the nucleation energy barrier. This should then be
311   reflected in an enhanced nucleation rate. To study such an influence on lens formation,
312   we performed several series of MD simulations. However, under none of these conditions
313   LRAT-Nt significantly enhanced the rate of lens formation (data not shown).

314

N-terminus of LRAT exhibits affinity for retinyl esters *in vitro*

316   To study the affinity of the LRAT N-terminus to RP *in vitro*, we synthesized the LRAT-Nt
317   peptide and assessed its recruitment to RP vs. TOG interface. Oil-in-water droplets were
318   formed and the peptide was added (Fig. 7A). Recruitment of the peptide to the droplet
319   interface will decrease the interfacial surface tension (Fig. 7A) (Ajjaji et al., 2019; Small,
320   Wang, & Mitsche, 2009), which happened for both RP and TOG (Fig. 7B). Tension
321   reached an equilibrium value which corresponds to the maximum of adsorbed peptides
322   (9.2 mN/m for TOG, and 6.1 mN/m for RP). The peptide recruitment level is determined
323   by the neutral lipid affinity for LRAT-Nt. To further investigate this, we performed a rapid
324   compression experiment whereby, at the equilibrium interfacial tension, the droplet
325   interface was reduced by decreasing its volume (Fig. 7C,D, left, dotted lines). This
326   operation transiently increased the interfacial lateral pressure, *i.e.* the peptide surface
327   density, and we recorded the relaxation of the system to equilibrium. During compression,
328   surface tension decreased in the case of TOG, reached a transient plateau and
329   subsequently continued decreasing (Fig. 7C). Appearance of the plateau is a signature of
330   a rearrangement of the peptide at the surface, induced by the increase of its surface
331   density (Mitsche & Small, 2013). As soon as compression was stopped, surface tension
332   increased again, which is a signature of the desorption of some of the peptides from the
333   surface. This behavior at the TOG interface is unique to LRAT-Nt, as the 11mer repeat
334   domain of Plin1 does not show such response under similar experimental procedures
335   (Ajjaji et al., 2019). With RP, compression led to a continuous decrease of tension (Fig.
336   7D) and upon arrest of compression, tension remained constant: the peptide did not
337   desorb from the interface. These results confirm the MD simulations and show that the
338   LRAT-Nt peptide interacts with neutral lipids and with a preference for retinyl esters.

339

Discussion

340
341 Lipid droplet formation starts when neutral lipids accumulate within the bilayer of
342 biological membranes above the a critical demixing concentration (Thiam and Forêt,
343 2016; Walther et al., 2017). Although the intrinsic capacity of different classes of neutral
344 lipids to form LDs is well accepted based on biophysical considerations (Ben M'barek et
345 al., 2017), *in vivo* this has only been demonstrated for triacylglycerols in yeast (Sandager
346 et al., 2002). As cholesteryl ester synthesizing enzymes also contribute to TAG synthesis,
347 it remains to be established whether cholesteryl esters are capable of forming lipid
348 droplets in the absence of triacylglycerols (Sandager et al., 2002). Here we show the
349 existence of an alternative route for LD biogenesis, in which synthesis of another class of
350 neutral lipids, retinyl esters, is sufficient to drive LD formation.
351 Based on biophysical properties of retinyl esters, we show that the spontaneous
352 nucleation of retinyl ester-generated LDs is somewhat less efficient as compared to TAGs.
353 Indeed, molecular dynamic simulations (Fig. 3 A,B) and *in vitro* experiments measuring
354 the tension of artificial droplet interfaces (Table 1) suggest that RP droplets have a higher
355 nucleation barrier, or lower nucleation efficiency than TAGs. Despite these biophysical
356 considerations, retinyl ester-filled LDs are efficiently formed upon exogeneous induction
357 of LRAT in yeast cells that lack the machinery to synthesize TAG/SE-filled LDs (Fig. 2).
358 Surprisingly, the LRAT protein itself is involved in the generation of the large sized LDs
359 that are characteristic for retinyl ester-containing LDs.
360
361 LRAT is broadly expressed with highest expression levels in the intestine, liver, testis and
362 eye (Liu and Gudas, 2005; Ruiz et al., 1999). The majority of dietary vitamin A (~75%) is,
363 however, taken up by hepatocytes (Gottesman et al., 2001) and stored as retinyl esters in
364 the liver, primarily in hepatic stellate cells (Blaner et al., 2009; Blomhoff et al., 1991;
365 Friedman, 2008; Gottesman et al., 2001; Ross and Zolfaghari, 2004). LRAT expression is
366 the highest in quiescent HSCs (Fig. 1E), in agreement with previous reports (Mederacke
367 et al., 2013), but this expression is rapidly lost upon activation of HSCs. LRAT
368 expression thus coincides with the presence of large LDs in quiescent HSCs. When LRAT
369 expression is reduced (in activated HSCs, Fig. 1E) or absent in LRAT$^{-/-}$ mice (Ajat et al.,
370 2017; O'Byrne et al., 2005), HSCs lack their characteristic large LDs. These findings
371 show that the presence of LRAT correlates with the existence of the large LDs, consistent
372 with the data now presented here.
373
374 LRAT belongs to the papain-like or NlpC/P60 thiol protease superfamily of proteins
375 (Anantharaman and Aravind, 2003). The H-RAS-like suppressor (HRASLS) enzymes,
376 also known as LRAT-like proteins comprise a vertebrate subfamily that includes LRAT
377 and that function in acyl chain remodeling of phospholipids (Golczak et al., 2012;
378 Mardian et al., 2015). The *in vivo* biological substrates and activities of most family
379 members have not yet been elucidated. LRAT is the best characterized family member,
380 which catalyzes the formation of retinyl esters by transferring an acyl group from the *sn-1*
381 position of PC onto ROH. The substrate specificity of LRAT for PC as acyl donor is
382 intriguing. LD size is regulated by several factors including PC synthesis (Krahmer et al.,
383 2011). During LD growth, the expanding LD monolayer activates CTP:Phosphocholine
384 cytidylyltransferase, a key enzyme in PC synthesis. LRAT degrades PC which may result
385 in activation of the same PC synthesizing pathway. Alternatively, reduced PC

11

386 concentrations may either destabilize LDs and induce coalescence of LDs or increase ER
387 bilayer tension, thereby generating larger (merged) LDs. Concomitant with retinyl ester
388 production, however, PC is converted to lyso-PC. The bilayer surface tension is reduced
389 by lyso-phospholipids, facilitating LD budding and reducing LD size (Ben M'barek et al.,
390 2017). Thus, counteracting forces contributing to LD size are involved in the generation
391 of retinyl ester-loaded LDs. The N-terminus of LRAT tips the balance as it is required for
392 the generation of large LDs in mammalian cells. The effect of the N-terminus of LRAT on
393 LD size is specific for retinyl ester-mediated LD formation: despite its presence in
394 CHO-k1 LRAT-GFP cells, it does not affect the size of TAG filled LDs (Fig. 4).
395 Since the N-terminus of LRAT does not seem to affect the rate of LD formation, it could
396 change the thermodynamic equilibrium and decreases the nucleation concentration. As a
397 result, it would then also dictate where LD formation occurs. However, we did not
398 observe a colocalization of LRAT with nascent LDs (data not shown). Therefore, we
399 consider it more likely that the observed specific affinity of the LRAT N-terminus for
400 retinyl esters is likely to play an important role in affecting LD size, for example by
401 changing the membrane topology of LRAT. LRAT is anchored to the ER membrane by a
402 single transmembrane spanning domain at the C-terminus and with the catalytic domain
403 and the N-terminus oriented towards the cytoplasm (Moise et al., 2007). The production
404 of retinyl esters results in a strongly enhanced membrane binding of the N-terminus as
405 illustrated by the deeper embedding of the N-terminus in the membrane, combined with
406 the specific interaction with retinyl esters. Indeed, in the absence of the N-terminus,
407 LRAT maintains retinyl ester production but fails to generate large LDs. In addition to a
408 direct interaction with retinyl esters, it can however not be excluded that the N-terminus
409 of LRAT also affects lipid droplet size by interfering with other mechanisms such as
410 lipolysis and/or lipogenesis.
411 In summary, the molecular design of LRAT is well suited to store retinyl esters in LDs.
412 With its C-terminal transmembrane domain, LRAT is anchored in the endoplasmic
413 reticulum and directs newly synthesized retinyl esters in the lipid bilayer. The retinyl
414 esters have the intrinsic capacity to form lipid droplets and with the N-terminal
415 hydrophobic peptide LRAT specifically affects the size of retinyl ester-loaded lipid
416 droplets.
417
418
419

Acknowledgments

We thank Shreyas Sinha and Elmon Meijering for their assistance during the initial phase of experiments. Microscopy images were acquired at the Center of Cellular Imaging, Faculty of Veterinary Medicine, Utrecht University, we thank Esther van 't Veld for the technical assistance. Lipid analyses were performed at the Lipidomics Centre, Faculty of Veterinary Medicine, Utrecht University, we thank Jeroen Jansen for the technical assistance.

Author Contributions

Conceptualization: J.B.H.; Methodology: M.R.M., T.A.W., A.R.T., W.A.P., J.B.H.; Software: T.A.W.; Formal Analysis: M.R.M., T.A.W.; Investigation: M.R.M., T.A.W., K.K.Y., A.T., M.C.M., L.C., A.C., M.W.H.; Writing – Original Draft: M.R.M., J.B.H.; Writing – Review & Editing: M.R.M., M.H., A.B.V., A.R.T., W.A.P., J.B.H.; Visualization: M.R.M., T.A.W., K.K.Y., M.C.M., L.C., A.C., R.W.W.; Supervision: M.H., A.B.V., F.R., A.R.T., W.A.P., J.B.H.; Project Administration: J.B.H.

Declaration of Interests

The authors declare no competing interests.

Material & Methods

Hepatic stellate cells isolation and cell culturing

Hepatic stellate cells (HSCs) were isolated from 10–12 week-old male mice (C57BL/6J background, wild-type pubs from crossed LRAT$^{+/-}$ heterozygote (Liu and Gudas, 2005 mice) as described before (Riccalton-Banks et al., 2003). Animals were handled according to governmental and international animal experimentation guidelines and laws. Experiments were approved by the Animal Experimentation Committee (Dierexperimentencommissie; DEC) of Utrecht University (DEC number 2013.III.02.016). After isolation, cells were protected from light and cultured on coverslips in 24-wells plates (Nunc, Roskilde, Denmark) in Dulbecco Modified Eagle Medium (DMEM) supplemented with 10% fetal bovine serum (FBS), 100 U/mL penicillin and 100 μg/mL streptomycin (all obtained from Gibco, Invitrogen GmbH, Lofer, Germany.

CHO-k1 cells were cultured in Ham's F-12 medium supplemented with 7.5% FBS, 100 units/ml penicillin, and 100 μg/mL streptomycin. The human hepatic stellate cell line LX-2 cells (kindly donated by Dr. Friedman (New York, NY, USA)) were grown in DMEM containing 10% FBS, 100 U/mL penicillin and 100 μg/mL streptomycin. All cells were maintained in a humidified incubator (5% CO2) at 37 °C. Depending on the experiment, cells were incubated with retinol (Sigma, stocks of 30 mM in EtOH), oleic acid (Sigma) coupled to fatty acid free-BSA (Sigma, stocks of 10 mM fatty acid in 12% BSA) and/or triacsin C (Cayman, stocks of 1 mg/mL in DMSO).

Retinol handling

Retinol (Sigma) was dissolved in ethanol (30 mM) and stored in 50 μL aliquots at -80°C. We routinely measured UV absorption spectra of retinol stocks before use and calculated the current stock concentration by making use of the molar extinction coefficient of retinol in EtOH (52,480 mol L^{-1} cm^{-1} at 325 nm) (Ross AC, 1981). In addition, we made use of the observation that after exposure to UV-light, a peak around 240 nm emerged, accompanied with a decrease around 325 nm. We routinely monitored E_{325}/E_{240} ratios and used exclusively stocks with a ratio of 5 or higher, which was estimated to correspond with a retinol integrity of about 70%.

Generation of stable cell lines

Human LRAT cDNA was synthesized and cloned into a pcDNA3.1(+) vector (Clontech, Palo Alto, California, USA) by a third party (GeneArt, Thermo Fisher Scientific, Waltham, MA, USA). In addition, the LRAT sequence was cloned into a pEGFP-N2 vector (Clontech), resulting in LRAT fused to the N-terminus of GFP. The construct coding for the deletion mutant (ΔNt-LRAT-GFP) was generated by site directed mutagenesis (New England Biolabs, Ipswich, MA). CHO-k1 and LX-2 cells were transiently transfected by Lipofectamine 2000 (Thermo Fisher) according to the manufacturer's instructions. Stable CHO-k1 cells expressing the various LRAT variants or control GFP were generated as follows. Cells (2x10^6) were electroporated in PBS with 15 μg DNA and a pulse of 260 V. After plating, cells were cultured for 48h in the absence and for 3 weeks in the presence of 1 mg/mL G-418 selection antibiotic (Thermo Fisher). Stable cells expressing GFP-fusion proteins were trypsinized and single GFP$^+$ cells with

14

486   scatter properties (FSC and SSC) similar to their non-transfected counterparts were plated
487   into 96-wells plates by FACS (Influx Cell Sorter, BD Biosciences). A GFP-negative gate
488   was chosen to select monoclonal stable cells expressing non-fluorescent proteins. After
489   plating, the monoclonal cells were allowed to grow until wells reached confluency.
490   Clones with comparable morphology as compared to parental CHO-k1 cells (cell size,
491   nucleus, lipid droplets) were selected. The absence or presence of LRAT enzymatic
492   activity in LRAT, GFP, LRAT-GFP and ΔNt-LRAT-GFP expressing clones was confirmed
493   by determination of retinyl esters (see below) and UV⁺-autofluorescent lipid droplets in
494   combination with GFP-fluorescence by FACS (FACSCanto II, BD Biosciences) after
495   incubation of cells with retinol.
496
497   **Confocal microscopy of mammalian cells**
498   Cells were plated on Lab-Tek II 8-chamber slides (Thermo Fisher) and incubated as
499   described in the figure legends. Cells were fixed in 4% paraformaldehyde (Electron
500   Microscopy Sciences Hatfield, PA, USA). Subsequently, cells were stained with either
501   DAPI, BODIPY 493/503 (Thermo Fisher), and/or LD540 (kindly donated by Dr. C.
502   Thiele, Bonn, Germany) (Spandl et al., 2009). Staining for immunofluorescence was
503   performed with anti-desmin or anti-α smooth muscle actin (both from Thermo Scientific),
504   followed by goat-anti-mouse-alexa647 or donkey-a-rabbit-alexa647 (Life Technologies,
505   Paisley, UK). Cells were mounted with FluorSave (Calbiochem, Billerica, MA, USA) and
506   subsequently imaged with a Leica TCS SPE Laser Scanning Spectral Confocal
507   Microscope (Wetzlar, Germany) or a Nikon A1R confocal microscope (Amsterdam, The
508   Netherlands) using preset settings for the representative dyes. For the detection of
509   retinoid autofluorescence, presets for DAPI were used.
510
511   **Quantification of cells with lipid droplet parameters**
512   To quantify cells and lipid droplets, z-series of cells were imaged in tile-scan mode.
513   Datasets were generated with either CellProfiler v2.2.0 (Kamentsky et al., 2011) or Imaris
514   v8.2.0 (Bitplane, Belfast, Northern Ireland), both resulting in the identification of lipid
515   droplets associated with individual cells. Data were subsequently expressed for individual
516   cells containing 'cell size' (diameters of cells, in arbitrary units), 'number of lipid droplets
517   per cell', 'mean lipid droplet volume per cell' (mean of all LD diameters of the cell to the
518   3rd power, in arbitrary units) and 'total lipid droplet volume per cell' (product of 'number
519   of lipid droplets per cell' and 'mean lipid droplet volume per cell', in arbitrary units).
520   Subsequently, the resulting data were processed with R v3.4.4 and RStudio v1.0.153
521   using R-packages 'openCyto' v1.14.0, 'reshape2' v1.4.2 and 'ggplot2' v2.2.1.
522   To analyze the lipid droplet size distribution, lipid droplet diameters were not linked to
523   individual cells, but analyzed per condition. Ranges of LD-diameter bins were calculated
524   using the limits of the first, second, third, fourth and fifth diameter quintile of all lipid
525   droplets. LD-presence in each bin was counted per condition and expressed as percentage
526   (all lipid droplets per condition were set to 100%).
527
528   **Structured illumniation microscopy (3D-SIM)**
529   After treatment, cells were stained with DAPI and HCS LipidTOX Red Neutral Lipid
530   Stain (Thermo Fisher) and mounted with Vectashield Antifade Mounting Medium (Vector
531   Laboratories, Burlingame, CA, USA). Structured illumniation microscopy was performed

532 using a Deltavision OMX-V4 Blaze (GE Healthcare, Chicago, IL, United States) setup
533 equipped with 4 sCMOS (PCO) cameras. Immersion oil with 1.516 refractive index (GE
534 Healthcare) was placed on the 60x objective (Olympus U-PLAN APO, NA 1.42).
535 Fluorophores were excited with a diode 405 nm (Vortran Stradus, 100 mW) and an OPSL
536 568 nm (Coherent , 100 mW) laser modulated to 1% by Neutral density filters. System
537 supplied filter blocks were used to acquire fluorescence of DAPI (Ex: 382-409, Em:
538 421-450) and LipidTOX Red (Ex: 561-580, Em: 591-627). Raw images were processed
539 using SoftWoRx software (GE Healthcare) with system OTFs pre-determined with 100
540 nm fluorescent polystyrene beads (Thermo scientific) and camera alignment parameters
541 for the different channels (see supplemental materials). Acquired images were
542 deconvolved using default settings (omitting Wiener filtering and background subtraction)
543 including negative values (supplied as such in supplemental data) and intensities were
544 linearly adjusted. Images in the figures are supplied as maximum intensity projections
545 (movies are in supplemental data).
546
547 **Lecithin:retinol acyltransferase activity assay**
548 Lecithin:retinol acyltransferase activity in homogenates expressing various LRAT
549 variants was performed as described previously (Golczak et al., 2015). Briefly, cells were
550 cultured overnight in T-75 culture flasks (CELLSTAR, Greiner Bio-One GmbH,
551 Frick-enhausen, Germany) under normal cell growth conditions. After scraping in
552 ice-cold PBS, cells were homogenized on ice with 26-gauge needles (BD Bioscience, San
553 Jose, CA, USA). Homogenates containing 200 μg total protein were mixed with reaction
554 mix containing 5 mM DTT, 5 mM EDTA, 10 mM Tris-HCl (pH 8.0), 1% BSA, 0.2 μM
555 ascorbic acid, 2 mM PC(7:0/7:0) and increasing amounts of retinol. Subsequently,
556 mixtures were incubated for 60 min at 37oC in amber glass vials. Levels of retinyl
557 heptanoate were determined by LC-MS/MS (see below). K_m en v_{max} values were
558 estimated using Michaelis-Menten kinetics.
559
560 **Retinoids and neutral lipid determination by LC-MS/MS**
561 Lipids were extracted as previously described (Bligh and Dyer, 1959). To avoid
562 photo isomerization and oxidation of the retinoids, extractions were performed under red
563 light and in amber tubes. In addition, 1 nmol butylated-hydroxytoluene was added to
564 every sample. As internal standard, 250 pmol of retinyl acetate in MeOH/CHCl$_3$ (1:1, v/v)
565 was added. The combined chloroform phases were dried under nitrogen and stored at
566 − 20 °C until further analysis.
567 Extract were dissolved in MeOH/CHCl3 (1:1) and stored in amber autosampler vials. To
568 measure retinoids, samples were injected and separated on a 250×3.0 mm Synergi™ 4u
569 Max-RP 80A column (4 μm particle size, Phenomenex, CO, USA) with a flow rate of
570 350 μL min^{-1}. To this end, a gradient (solvent A; acetonitrile:water (95:5), solvent B;
571 acetone:chloroform (85:15), 0 min; 90% A, 5 min; 40% A, 17 min; 0% A, 19 min; 90% A,
572 25 min; 90% A) was generated by a Flexar UHPLC system (Perkin Elmer, Waltham, MA,
573 USA). The column outlet was connected to a triple quadrupole mass spectrometry (API
574 4000 QTRAP, MDS Sciex/Applied Biosystems, Foster City, Canada) with an atmospheric
575 pressure chemical ionization (APCI) ionization source (set to 500 °C). Multiple reaction
576 monitoring (MRM) in positive ion mode was used to detect retinyl ester species with
577 settings and m/z transitions as described before (Ajat et al., 2017). Chromatographic

578 peaks were integrated and quantified using Analyst software version 1.4.3 (Applied
579 Biosystems, Foster City, Canada).
580 To measure other neutral lipids (sterols, triacylglycerols, steryl esters), samples were
581 injected and separated on a Kinetex/HALO C8 column (2.6 μm, 150 × 3.00 mm;
582 Phenomenex, Torrance, CA, USA). A gradient of methanol:H_2O (5:5 v/v, solvent A) and
583 methanol:isopropanol (8:2 v/v, solvent B) was generated by an Infinity II 1290 UPLC
584 (Agilent, Santa Clara, CA, USA) and with a constant flow rate of 600 μL min^{-1} (0 min;
585 100% A, 2 min; 0% A, 8 min; 0% A, 8.5 min; 100% A, 10 min; 100% A). Lipids were
586 measured using APCI in positive mode coupled to an Orbitrap Fusion mass spectrometer
587 (Thermo Scientific, Waltham, MA, USA). Vendor data files were converted to
588 mzML-format with msConvert (part of ProteoWizard v3.0.913) and processed with
589 XCMS Online v3.7.0 (Tautenhahn et al., 2012).
590

591 **Growth and fluorescence microscopy of yeast**
592 Yeast strains and plasmids used in this study are described in Supplemental Table 1. Yeast
593 were grown at 30°C in synthetic complete media containing 0.67% yeast nitrogen base
594 without amino acids (United States Biological), 2% glucose, and an amino acid mix
595 (United States Biological). Retinol (Sigma-Aldrich) was added to the medium at 4 mM
596 together with 1% Igepal CA-630 (Sigma-Aldrich). Cells were stained with 0.5 μg/ml
597 BODIPY 493/503 (Invitrogen) for 10 min and being washed once with phosphate
598 buffered saline.
599 Yeast were imaged at 30 °C in an Environmental Chamber with a DeltaVision Spectris
600 (Applied Precision Ltd.) comprising a wide-field inverted epifluorescence microscope
601 (IX70; Olympus), a 100 Å~ NA 1.4 oil immersion objective (UPlanSAPO; Olympus),
602 and a charge-coupled device Cool-Snap HQ camera (Photometrics).
603

604 **Western blot analysis**
605 Cells expressing LRAT-GFP and ΔN-LRAT-GFP were growth to logarithmic growth
606 phase and 10 OD600 units of cells were washed once with H_2O and lysed with glass beads
607 in a Precellys 24 homogenizer (Bertin Instruments). The lysate was cleared by
608 centrifugation at 500 $x\ g$ for 10 minutes at 4°C. The protein concentration of the lysate
609 was determined using a Bradford assay (Thermo Scientific) and 10 μg of protein were
610 separated by 4–12% of SDS-PAGE gel (Invitrogen), and transferred to nitrocellulose
611 membranes at 120 V for 2 h. The membrane was analyzed using primary antibodies to
612 GFP (1:1,000; Roche) and anti-porin (1:1,000; Invitrogen). Proteins were visualized using
613 IRDye secondary anti-mouse antibody (Li-COR Biosciences; 1:10,000). The blots were
614 visualized with an Odyssey infrared imaging system (Li-COR Biosciences).
615

616 **LRAT mRNA expression by quantitative PCR**
617 Expression of LRAT mRNA was determined as described (Tuohetahuntila et al., 2017).
618 Briefly, RNA was isolated with a RNeasy Micro Kit (Qiagen, Venlo, The Netherlands)
619 and cDNA was synthesized with an iScript cDNA Synthesis Kit (Bio-Rad). PCR
620 amplifications were performed using a Bio-Rad detection system with iQ SYBR Green
621 Supermix (Bio-Rad, Veenendaal, The Netherlands). Gene expression was normalized
622 against reference genes, sequences of the primers are listed in Suppl. Table 2.

Molecular dynamics

MD simulations were set up and run using the DAFT protocol (Wassenaar et al., 2015a), according to procedures for building membrane/solvent systems using INSANE (Wassenaar et al., 2015b) and for generating membrane/solvent/protein systems as described in (Wassenaar et al., 2015a). The latter comprises a step for the generation of the LRAT-Nt peptide (sequence MKNPMLEVVSLLLEKLLLISNFTLFSSGAAGEDKGRNSF; secondary structure LLLLHHHHHHHHHHHHHHHHHLLLLLLLLLLLLLLLLLLLL) or the CCTα P2 peptide (sequence VEEKSIDLIQKWEEKSREFIGSFLEMFG; secondary structure HHHHHHHHHHHHHHHHHHHHHHHHHHHHH), which was placed horizontally above the membrane. For docking simulations, the helix was placed at a distance 4 nm from the bilayer center with random rotation around the helix axes, while for assessment of the effect on lens formation speed, the helix was placed at 2.5 nm from the bilayer center, with the hydrophobic side facing towards the membrane. Simulations were performed using the coarse grain Martini 2.2 model (Marrink et al., 2004, 2007; Monticelli et al., 2008).
Simulations for assessing binding of LRAT-Nt AH to membranes with different compositions were set up in a hexagonal prism unit cell with a total number of 250 lipids per leaflet and a height of 9 nm. Simulations for assessing the lens forming propensity and speed, were set up in a hexagonal prism unit cell with base length of 24 nm and height of 10 nm, regardless of the presence or absence of protein. Numbers or ratios or lipids were set as described in the main text. All simulations were performed using Gromacs 2018.x (Pronk et al., 2013), using the automated Martini workflow *martinate* (Wassenaar et al., 2013).

Electron Microscopy

Yeast cells were grown in synthetic drop-out media lacking leucine at 30°C to an OD_{600} of approximately 0.6. IGEPAL (Sigma-Aldrich) was added to the cell cultures to a final concentration of 1%, prior to addition of retinol (Sigma-Aldrich) to a final concentration of 2 mM. Cells were then incubated for 10 min at 30°C before being processed for electron microscopy as follow. Cells were chemically fixed, embedded with 12% gelatin, cryo-sectioned and stained as previously described (Griffith et al., 2008). Sections were imaged in a FEI CM100bio electron microscope at 80 KV, equipped with a digital camera (Morada; Olympus). Two different grids with sections obtained from the same preparation were statistically evaluated by counting 75 randomly selected cell profiles before determining the average number of lipid droplets per cell section plus standard deviation between the two grids.

Monolayer tension measurements

Tension measurements were performed using a drop tensiometer device (Tracker, Teclis-IT Concept, France) (Ben M'barek et al., 2017). The principle of the drop profile analysis is based on the determination of the shape of a liquid drop suspended in another liquid form from a video image and its comparison with theoretical profiles calculated from the Gauss Laplace equation. The retinyl palmitate (Sigma, R-1512) drop (neutral

669 lipid phase), with or without containing the DOPC phospholipid, was formed in buffer
670 (50mM HEPES, 120mM potassium acetate, 1mM magnesium chloride, pH 7.4) at room
671 temperature. The tension was allowed to stabilize for a few minutes (it decreases by the
672 continuous absorption of phospholipids to the oil/water interface). Then, the drop is
673 compressed by decreasing its volume, until complete saturation of the interface is reached
674 (marked by a plateau of tension during compression).

675

676 **Droplet interface bilayer (DIB) experiments**
677 The DIB experiments was performed following the previous study of (Ben M'barek et al.,
678 2017). An oil phase containing phospholipids was prepared first. DOPC, DOPE and
679 DOPA were purchased from Avanti Polar Lipids, Inc. Lipids were mixed to the RP
680 (Sigma, R-1512) oil at a final lipid concentration of 0.2% w/w (about 10% chloroform
681 was in the final mixture in the case of DOPC initial stabilization of the DIBs, and we let it
682 evaporate over time; for the other phospholipids, chloroform was evaporated prior to
683 addition of RP). Then, an emulsion was prepared mixing the buffer with RP (1:5 v/v).
684 Finally, the same volumes of emulsion and phospholipids in RP were put together, and
685 the resulting emulsion was placed on a hydrophobic coverslip.

686

687 **Interfacial tension measurements**
688 A pendent droplet tensiometer designed by Teclis Instruments (Longessaigne, France)
689 was used to measure the interfacial tension of oil/water interfaces. All experiments were
690 conducted at room temperature. To create oil/buffer interfaces, oil drops (10μL) were
691 formed at the tip of a J-needle submerged in 5 mL of HKM buffer.

692 *Oil-peptide surface tension measurement:* 10 μl of LRAT peptide solution in DMSO was
693 added to the bulk buffer while the tension of trioleoylglycerol/buffer or retinyl
694 palmitate/buffer interface was measured. The resulting concentration of peptide was 4.6
695 μM for both retinyl palmitate and trioleoylglycerol experiments. Oil-peptide surface
696 tension was determined when the interfacial tension was stabilized.
697 After tension stabilization, the interface is compressed. The compression was then
698 stopped, and area was kept constant as interfacial tension was recorded. Relaxation of the
699 tension was observed only for trioleoylglycerol/buffer interfaces. Human LRAT peptide
700 (AA 1-39) was synthesized by Bio-Synthesis (Lewisville, Texas, USA).
701

702 **Statistical analyses**
703 All figures were built in RStudio v1.0.153 (R v3.4.4) and processed in Inkscape v0.92.2.
704 Barplots represent means ± standard deviation (SD) or standard error of the mean (SEM)
705 as indicated in the figure legends. Statistical significance was determined by two-tailed
706 paired or unpaired Welch's t-test or Wilcoxon rank sum test, or by Pearson's Chi-squared
707 test, as indicated. In experiments with multiple testing, P-values were corrected by the
708 Benjamini-Hochberg procedure. P-values below 0.05 were considered statistically
709 significant.

710

711

References

712

713 Ajat, M., Molenaar, M., Brouwers, J.F.H.M., Vaandrager, A.B., Houweling, M., and
714 Helms, J.B. (2017). Hepatic stellate cells retain the capacity to synthesize retinyl esters
715 and to store neutral lipids in small lipid droplets in the absence of LRAT. Biochim.
716 Biophys. Acta *1862*, 176–187.

717 Ajjaji, D., Ben M'barek, K., Mimmack, M.L., England, C., Herscovitz, H., Dong, L., Kay,
718 R.G., Patel, S., Saudek, V., Small, D.M., et al. (2019). Dual binding motifs underpin the
719 hierarchical association of perilipins1-3 with lipid droplets. Mol. Biol. Cell *30*, 703–716.

720 Anantharaman, V., and Aravind, L. (2003). Evolutionary history, structural features and
721 biochemical diversity of the NlpC/P60 superfamily of enzymes. Genome Biol. 1–12.

722 Ben M'barek, K., Ajjaji, D., Chorlay, A., Vanni, S., Forêt, L., and Thiam, A.R. (2017).
723 ER Membrane Phospholipids and Surface Tension Control Cellular Lipid Droplet
724 Formation. Dev. Cell *41*, 591–604.e7.

725 Bigay, J., Casella, J.-F., Drin, G., Mesmin, B., and Antonny, B. (2005). ArfGAP1
726 responds to membrane curvature through the folding of a lipid packing sensor motif.
727 EMBO J. *24*, 2244–2253.

728 Blaner, W.S., O'Byrne, S.M., Wongsiriroj, N., Kluwe, J., D'Ambrosio, D.M., Jiang, H.,
729 Schwabe, R.F., Hillman, E.M.C., Piantedosi, R., and Libien, J. (2009). Hepatic stellate
730 cell lipid droplets: a specialized lipid droplet for retinoid storage. Biochim. Biophys. Acta
731 *1791*, 467–73.

732 Bligh, E.G., and Dyer, W.J. (1959). A rapid method of total lipid extraction and
733 purification. Can. J. Biochem. Physiol. *37*, 911–917.

734 Blomhoff, R., Green, M.H., Green, J.B., Berg, T., and Norum, K.R. (1991). Vitamin A
735 metabolism: new perspectives on absorption, transport, and storage. Physiol. Rev. *71*,
736 951–990.

737 Boumann, H.A., Gubbens, J., Koorengevel, M.C., Oh, C.-S., Martin, C.E., Heck, A.J.R.,
738 Patton-Vogt, J., Henry, S.A., de Kruijff, B., and de Kroon, A.I.P.M. (2006). Depletion of
739 phosphatidylcholine in yeast induces shortening and increased saturation of the lipid acyl
740 chains: evidence for regulation of intrinsic membrane curvature in a eukaryote. Mol. Biol.
741 Cell *17*, 1006–17.

742 Chelstowska, S., Widjaja-Adhi, M.A.K., Silvaroli, J.A., and Golczak, M. (2017). Impact
743 of LCA-Associated E14L LRAT Mutation on Protein Stability and Retinoid Homeostasis.
744 Biochemistry (Mosc.) *56*, 4489–4499.

745 Chorlay, A., and Thiam, A.R. (2018). An Asymmetry in Monolayer Tension Regulates
746 Lipid Droplet Budding Direction. Biophys. J. *114*, 631–640.

747 Choudhary, V., Ojha, N., Golden, A., and Prinz, W.A. (2015). A conserved family of
748 proteins facilitates nascent lipid droplet budding from the ER. J. Cell Biol. *211*, 261–271.

749 Deslandes, F., Thiam, A.R., and Forêt, L. (2017). Lipid Droplets Can Spontaneously Bud
750 Off from a Symmetric Bilayer. Biophys. J. *113*, 15–18.

751 Friedman, S.L. (2008). Hepatic Stellate Cells : Protean , Multifunctional , and Enigmatic
752 Cells of the Liver. Phys. Rev. 125–172.

753 Gautier, R., Douguet, D., Antonny, B., and Drin, G. (2008). HELIQUEST: a web server
754 to screen sequences with specific alpha-helical properties. Bioinforma. Oxf. Engl. *24*,
755 2101–2102.

756 Golczak, M., Kiser, P.D., Sears, A.E., Lodowski, D.T., Blaner, W.S., and Palczewski, K.
757 (2012). Structural basis for the acyltransferase activity of lecithin:retinol
758 acyltransferase-like proteins. J. Biol. Chem. *287*, 23790–807.

759 Golczak, M., Sears, A.E., Kiser, P.D., and Palczewski, K. (2015). LRAT-specific domain
760 facilitates vitamin A metabolism by domain swapping in HRASLS3. Nat. Chem. Biol. *11*,
761 26–32.

762 Gottesman, M.E., Quadro, L., and Blaner, W.S. (2001). Studies of vitamin A metabolism
763 in mouse model systems. BioEssays *23*, 409–419.

764 Griffith, J., Mari, M., Mazière, A.D., and Reggiori, F. (2008). A Cryosectioning
765 Procedure for the Ultrastructural Analysis and the Immunogold Labelling of Yeast
766 Saccharomyces cerevisiae. Traffic *9*, 1060–1072.

767 Hashemi, H.F., and Goodman, J.M. (2015). The life cycle of lipid droplets. Curr. Opin.
768 Cell Biol. *33*, 119–124.

769 Hernandez-Gea, V., and Friedman, S.L. (2011). Pathogenesis of liver fibrosis. Annu. Rev.
770 Pathol. *6*, 425–56.

771 Igal, R.A., Wang, P., and Coleman, R.A. (1997). Triacsin C blocks de novo synthesis of
772 glycerolipids and cholesterol esters but not recycling of fatty acid into phospholipid:
773 evidence for functionally separate pools of acyl-CoA. Biochem. J. *324*, 529.

774 Jiang, W., and Napoli, J.L. (2012). Reorganization of cellular retinol-binding protein type
775 1 and lecithin:retinol acyltransferase during retinyl ester biosynthesis. Biochim. Biophys.
776 Acta *1820*, 859–869.

777 Kamentsky, L., Jones, T.R., Fraser, A., Bray, M.-A., Logan, D.J., Madden, K.L., Ljosa,
778 V., Rueden, C., Eliceiri, K.W., and Carpenter, A.E. (2011). Improved structure, function
779 and compatibility for CellProfiler: modular high-throughput image analysis software.
780 Bioinformatics *27*, 1179–1180.

781   Kassan, A., Herms, A., Fernández-Vidal, A., Bosch, M., Schieber, N.L., Reddy, B.J.N.,
782   Fajardo, A., Gelabert-Baldrich, M., Tebar, F., Enrich, C., et al. (2013). Acyl-CoA
783   synthetase 3 promotes lipid droplet biogenesis in ER microdomains. J. Cell Biol. *203*,
784   985–1001.

785   Khandelia, H., Duelund, L., Pakkanen, K.I., and Ipsen, J.H. (2010). Triglyceride blisters
786   in lipid bilayers: implications for lipid droplet biogenesis and the mobile lipid signal in
787   cancer cell membranes. PloS One *5*, e12811.

788   Kluwe, J., Wongsiriroj, N., Troeger, J.S., Gwak, G.-Y., Dapito, D.H., Pradere, J.-P., Jiang,
789   H., Siddiqi, M., Piantedosi, R., O'Byrne, S.M., et al. (2011). Absence of hepatic stellate
790   cell retinoid lipid droplets does not enhance hepatic fibrosis but decreases hepatic
791   carcinogenesis. Gut 1–10.

792   Krahmer, N., Guo, Y., Wilfling, F., Hilger, M., Lingrell, S., Heger, K., Newman, H.W.,
793   Schmidt-Supprian, M., Vance, D.E., Mann, M., et al. (2011). Phosphatidylcholine
794   synthesis for lipid droplet expansion is mediated by localized activation of
795   CTP:phosphocholine cytidylyltransferase. Cell Metab. *14*, 504–15.

796   Krahmer, N., Farese, R.V., and Walther, T.C. (2013). Balancing the fat: lipid droplets and
797   human disease. EMBO Mol. Med. *5*, 973–983.

798   Liu, L., and Gudas, L.J. (2005). Disruption of the lecithin:retinol acyltransferase gene
799   makes mice more susceptible to vitamin A deficiency. J. Biol. Chem. *280*, 40226–34.

800   MacDonald, P.N., and Ong, D.E. (1988). A lecithin:retinol acyltransferase activity in
801   human and rat liver. Biochem. Biophys. Res. Commun. *156*, 157–63.

802   Mardian, E.B., Bradley, R.M., and Duncan, R.E. (2015). The HRASLS (PLA/AT)
803   subfamily of enzymes. J. Biomed. Sci. *22*, 99.

804   Marrink, S.J., de Vries, A.H., and Mark, A.E. (2004). Coarse Grained Model for
805   Semiquantitative Lipid Simulations. J. Phys. Chem. B *108*, 750–760.

806   Marrink, S.J., Risselada, H.J., Yefimov, S., Tieleman, D.P., and de Vries, A.H. (2007).
807   The MARTINI force field: coarse grained model for biomolecular simulations. J. Phys.
808   Chem. B *111*, 7812–7824.

809   Mederacke, I., Hsu, C.C., Troeger, J.S., Huebener, P., Mu, X., Dapito, D.H., Pradere,
810   J.-P., and Schwabe, R.F. (2013). Fate tracing reveals hepatic stellate cells as dominant
811   contributors to liver fibrosis independent of its aetiology. Nat. Commun. *4*, 2823.

812   Moise, A.R., Golczak, M., Imanishi, Y., and Palczewski, K. (2007). Topology and
813   membrane association of lecithin: retinol acyltransferase. J. Biol. Chem. *282*, 2081–90.

814 Molenaar, M.R., Vaandrager, A.B., and Helms, J.B. (2017). Some Lipid Droplets Are
815 More Equal Than Others: Different Metabolic Lipid Droplet Pools in Hepatic Stellate
816 Cells. Lipid Insights *10*, 1178635317747281.

817 Monticelli, L., Kandasamy, S.K., Periole, X., Larson, R.G., Tieleman, D.P., and Marrink,
818 S.-J. (2008). The MARTINI Coarse-Grained Force Field: Extension to Proteins. J. Chem.
819 Theory Comput. *4*, 819–834.

820 Mitsche, M.A., and Small, D.M. (2013). Surface pressure-dependent conformation
821 change of apolipoprotein-derived amphipathic α-helices. J. Lipid Res. *54*, 1578–1588.

822 O'Byrne, S.M., Wongsiriroj, N., Libien, J., Vogel, S., Goldberg, I.J., Baehr, W.,
823 Palczewski, K., and Blaner, W.S. (2005). Retinoid absorption and storage is impaired in
824 mice lacking lecithin:retinol acyltransferase (LRAT). J. Biol. Chem. *280*, 35647–57.

825 Orland, M.D., Anwar, K., Cromley, D., Chu, C.-H., Chen, L., Billheimer, J.T., Hussain,
826 M.M., and Cheng, D. (2005). Acyl coenzyme A dependent retinol esterification by acyl
827 coenzyme A: diacylglycerol acyltransferase 1. Biochim. Biophys. Acta *1737*, 76–82.

828 Pol, A., Gross, S.P., and Parton, R.G. (2014). Review: biogenesis of the multifunctional
829 lipid droplet: lipids, proteins, and sites. J. Cell Biol. *204*, 635–46.

830 Prévost, C., Sharp, M.E., Kory, N., Lin, Q., Voth, G.A., Farese, R.V., and Walther, T.C.
831 (2018). Mechanism and Determinants of Amphipathic Helix-Containing Protein
832 Targeting to Lipid Droplets. Dev. Cell *44*, 73–86.e4.

833 Pronk, S., Páll, S., Schulz, R., Larsson, P., Bjelkmar, P., Apostolov, R., Shirts, M.R.,
834 Smith, J.C., Kasson, P.M., van der Spoel, D., et al. (2013). GROMACS 4.5: a
835 high-throughput and highly parallel open source molecular simulation toolkit. Bioinforma.
836 Oxf. Engl. *29*, 845–854.

837 Riccalton-Banks, L., Liew, C., Bhandari, R., Fry, J., and Shakesheff, K. (2003).
838 Long-term culture of functional liver tissue: three-dimensional coculture of primary
839 hepatocytes and stellate cells. Tissue Eng. *9*, 401–410.

840 Ross, A.C. (1981). Separation of long-chain fatty acid esters of retinol by
841 high-performance liquid chromatography. Anal. Biochem. *115*, 324–330.

842 Ross, A.C., and Zolfaghari, R. (2004). Regulation of Hepatic Retinol Metabolism:
843 Perspectives from Studies on Vitamin A Status. J. Nutr. *134*, 269S–275S.

844 Ruiz, A., and Bok, D. (2010). Focus on molecules: lecithin retinol acyltransferase. Exp.
845 Eye Res. *90*, 186–7.

846 Ruiz, a, Winston, A., Lim, Y.H., Gilbert, B.A., Rando, R.R., and Bok, D. (1999).
847 Molecular and biochemical characterization of lecithin retinol acyltransferase. J. Biol.
848 Chem. *274*, 3834–41.

849 Sandager, L., Gustavsson, M.H., Stahl, U., Dahlqvist, A., Wiberg, E., Banas, A., Lenman,
850 M., Ronne, H., and Stymne, S. (2002). Storage Lipid Synthesis Is Non-essential in Yeast.
851 J. Biol. Chem. *277*, 6478–6482.

852 Small, D.M., Wang, L., and Mitsche, M.A. (2009). The adsorption of biological peptides
853 and proteins at the oil/water interface. A potentially important but largely unexplored
854 field. J. Lipid Res. *50 Suppl*, S329-334.

855 Spandl, J., White, D.J., Peychl, J., and Thiele, C. (2009). Live cell multicolor imaging of
856 lipid droplets with a new dye, LD540. Traffic Cph. Den. *10*, 1579–84.

857 Tautenhahn, R., Patti, G.J., Rinehart, D., and Siuzdak, G. (2012). XCMS Online: a
858 web-based platform to process untargeted metabolomic data. Anal. Chem. *84*,
859 5035–5039.

860 Testerink, N., Ajat, M., Houweling, M., Brouwers, J.F., Pully, V.V., van Manen, H.J.,
861 Otto, C., Helms, J.B., and Vaandrager, A.B. (2012). Replacement of retinyl esters by
862 polyunsaturated triacylglycerol species in lipid droplets of hepatic stellate cells during
863 activation. PLoS ONE *7*.

864 Thiam, A.R., and Beller, M. (2017). The why, when and how of lipid droplet diversity. J.
865 Cell Sci. *130*, 315–324.

866 Thiam, A.R., and Forêt, L. (2016). The physics of lipid droplet nucleation, growth and
867 budding. Biochim. Biophys. Acta *1861*, 715–22.

868 Thoen, L.F.R., Guimarães, E.L.M., Dollé, L., Mannaerts, I., Najimi, M., Sokal, E., and
869 van Grunsven, L. a (2011). A role for autophagy during hepatic stellate cell activation. J.
870 Hepatol. *55*, 1353–1360.

871 Tuohetahuntila, M., Molenaar, M.R., Spee, B., Brouwers, J.F.J.F., Houweling, M.,
872 Vaandrager, A.B., and Helms, J.B.B. (2016). ATGL and DGAT1 are involved in the
873 turnover of newly synthesized triacylglycerols in hepatic stellate cells. J. Lipid Res. *57*,
874 1162–1174.

875 Tuohetahuntila, M., Molenaar, M.R., Spee, B., Brouwers, J.F.J.F., Wubbolts, R.,
876 Houweling, M., Yan, C., Du, H., VanderVen, B.C.B.C., Vaandrager, A.B., et al. (2017).
877 Lysosome-mediated degradation of a distinct pool of lipid droplets during hepatic stellate
878 cell activation. J. Biol. Chem. *292*, 12436–12448.

879   Vamparys, L., Gautier, R., Vanni, S., Bennett, W.F.D., Tieleman, D.P., Antonny, B.,
880   Etchebest, C., and Fuchs, P.F.J. (2013). Conical lipids in flat bilayers induce packing
881   defects similar to that induced by positive curvature. Biophys. J. *104*, 585–593.

882   Walther, T.C., and Farese, R.V. (2012). Lipid droplets and cellular lipid metabolism.
883   Annu. Rev. Biochem. *81*, 687–714.

884   Walther, T.C., Chung, J., and Farese, R.V. (2017). Lipid Droplet Biogenesis. Annu. Rev.
885   Cell Dev. Biol. *33*, 491–510.

886   Wassenaar, T.A., Ingólfsson, H.I., Priess, M., Marrink, S.J., and Schäfer, L.V. (2013).
887   Mixing MARTINI: electrostatic coupling in hybrid atomistic-coarse-grained
888   biomolecular simulations. J. Phys. Chem. B *117*, 3516–3530.

889   Wassenaar, T.A., Pluhackova, K., Moussatova, A., Sengupta, D., Marrink, S.J., Tieleman,
890   D.P., and Böckmann, R.A. (2015a). High-Throughput Simulations of Dimer and Trimer
891   Assembly of Membrane Proteins. The DAFT Approach. J. Chem. Theory Comput. *11*,
892   2278–91.

893   Wassenaar, T.A., Ingólfsson, H.I., Böckmann, R.A., Tieleman, D.P., and Marrink, S.J.
894   (2015b). Computational lipidomics with insane: A versatile tool for generating custom
895   membranes for molecular simulations. J. Chem. Theory Comput. *11*, 2144–2155.

896   Welte, M.A. (2015). Expanding roles for lipid droplets. Curr. Biol. *25*, R470–R481.

897

898

899 **Tables**

900

901 **Table 1.** Interfacial tension values by drop tensiometry

system	tension (mN/m)
TOG / H_2O	32
RP[1] / H_2O	8-14
TOG / DOPC / H_2O	0.5-0.6
RP[1] / DOPC / H_2O	0.08-0.2

902 *[1]based on density provided by manufacturer, 0.90-0.95 g/mL*

903

904

Figure Legends

Figure 1. *Lipid droplets containing retinyl esters have a distinct morphology.*
(A) Chemical structures of the neutral lipids retinyl palmitate, cholesteryl oleate, and trioleoylglycerol. **(B)** Reaction mechanism of LRAT. **(C,D)** Confocal microscopy of murine hepatic stellate cells (mHSCs) cultured for 1, 3, 6 or 8 days, stained with DAPI (blue), LD540 (green) and anti-desmin (red) **(C)**, or DAPI (blue) and anti-α-SMA (red) **(D)**. Scale bars indicate 50 μm. **(E)** Relative expression of LRAT mRNA in mHSCs after 1 or 7 days of culture by qPCR. Barplot indicates means ± SEM of 3 animals. Statistical significance was determined by a two-tailed paired Welch's t-test. **(F)** Confocal microscopy of mHSCs two hours after isolation, showing UV-autofluorescence (blue), LD540 (green) and anti-desmin (red). Bottom panel is a zoomed inset of the area surrounded by dotted lines in the main panel. Closed triangles indicate UV$^-$ LDs, open triangles indicate UV$^+$ LDs. Scale bars indicate 50 μm. **(G,H)** Confocal microscopy of CHO-k1 cells expressing GFP or LRAT-GFP, incubated overnight in the presence or absence of 20 μM ROH or 200 μM OA. Imaged channels are DAPI (blue) and LD540 (green) **(G)**, or UV-autofluorescence (left) and LD540 (middle) **(H)**. Scale bars indicate 10μm. **(I)** Full projections of 3D-SIM images of CHO-k1 cells expressing LRAT-GFP, incubated overnight in the presence 20 μM ROH or 200 μM OA. Bottom panels are zoomed insets of areas surrounded by dotted lines in the top panels. Scale bars indicate 10μm. * P < 0.05, ** P < 0.01, *** P < 0.001, NS: not significant.

Figure 2. *LRAT-mediated LD-formation in the absence of pre-existing LDs*
(A) Confocal microscopy of CHO-k1 expressing LRAT-GFP. After pre-incubation with medium containing 1% FBS, cells were incubated overnight with or without 200 μM OA or 20 μM ROH, in the presence or absence of 1 μg/mL triacsin C. Cells were stained with DAPI (blue) and LD540 (green). Scale bars indicate 10 μm. **(B)** Quantification of predominant RE-species by LC-MS/MS of wt and 4Δ yeast cells expressing LRAT, 2 hours after incubation in the presence or absence of 2 mM ROH. Amounts in pmol RE per μg protein. Barplot indicates means ± SD. **(C)** Wide-field microscopy of Erg6-mCherry expressing wt and 4Δ yeast cells, with or without expressing LRAT, 2 hours after incubation with or without 2 mM ROH ('—' or '+'). Images of UV-autofluorescence (green), Erg6-mCherry (red) and brightfield were taken. Scale bars indicate 5 μm. **(D)** Electron microscopy of wt and 4Δ yeast cells, with or without expressing LRAT, incubated with or without 2 mM ROH. ER, endoplasmic reticulum; LD, lipid droplet; M, mitochondria; N, nucleus. Scale bars indicate 250 nm.

(Cont. Fig. 2) **(E)** Electron microscopy of yft2Δscs3Δ, and 4Δ yeast cells expressing LRAT, incubated with 2 mM ROH. Scale bars indicate 100 nm. ER, endoplasmic reticulum (yellow lines in right panels); LD, lipid droplet (red lines right panels). **(F)** Wide-field microscopy of Erg6-mCherry expressing wt yeast cells expressing LRAT. Two time series of UV-autofluorescence (white), Erg6-mCherry (red) and brightfield, taken 2, 4, 6 and 8 minutes after addition of 2 mM ROH. Scale bars indicate 5 μm.

951 **Figure 3.** *Nucleation and budding properties of RE.*
952 **(A,B)** Coarse grain MD simulations of lens formation by 150 (18%) (A) and 250 (30%)
953 (B) neutral lipids per leaflet in a POPC membrane. Colors indicate the neutral lipid
954 composition, with marine for pure RE and red for pure TOG. The progress of lens
955 formation is shown as fractional loss of interactions between the neutral lipids and POPC
956 as function of time (log-scale). **(C)** Brightfield microscopy images of droplet interface
957 bilayers of droplets containing neutral lipid RP and lipid surfactants PC, PE or PA. Scale
958 bars indicate 20 μm. **(D)** Comparison of quantified budding angles (mean±SD) of
959 RP-containing droplets with lipid surfactants PC (176,2±2,8), PE (150,9±4,0) or PA
960 (129,5±5,7) vs. reported budding angles of TAG and SQ-containing droplets (Ben
961 M'barek et al., 2017). Barplot represent means of at least 8 individual measurements,
962 which are shown as black dots.
963

964 **Figure 4.** *Deletion of N-terminus of LRAT affects LD formation in CHO cells.*
965 **(A,B)** *In vitro* LRAT-activity of CHO-k1 homogenates expressing full-length or
966 ΔNt-LRAT-GFP. After incubation full-length LRAT-GFP with PC(7:0/7:0) and varying
967 concentration of ROH, ROH (peak a), RE(2:0) (internal standard, peak b) and RE(7:0)
968 (peak c) were measured by LC-MS/MS. MRM-transition 269/93 detects all retinoid
969 backbones (blue), whereas 399/269 specifically detects RE(7:0) (red) **(A)**.
970 RE(7:0)-synthesis by full-length or ΔNt-LRAT-GFP was normalized by GFP-levels of the
971 homogenates and plotted against increasing ROH concentrations. Estimated Km values
972 are indicated by vertical dashed lines. A representative plot of three independent
973 experiment is shown **(B)**. **(C,D)** Confocal microscopy of CHO-k1 cells expressing
974 LRAT-GFP or ΔNt-LRAT-GFP, incubated overnight in the presence or absence of 20 μM
975 ROH. Imaged channels are DAPI (blue) and LD540 (green) **(C)**, or UV-autofluorescence
976 (top) and LD540 (middle) **(D)**. Scale bars indicate 10 μm. **(E,F)** Quantification of cells
977 imaged by confocal microscopy. Cell sizes were plotted against total LD volume per cell
978 (LRAT-GFP or ΔNt-LRAT-GFP) and cells with similar total LD volumes per cell were
979 gated (black box, LRAT-GFP+OA: 12 cells; ΔNt-LRAT-GFP+OA: 40 cells;
980 LRAT-GFP+ROH: 13 cells; ΔNt-LRAT-GFP+ROH: 31 cells) **(E)**. The gated cells were
981 expressed as log-ratios of mean LD volume vs. LD number. Mean values (±SD) were
982 -1,96±1,34 (LRAT-GFP with OA); -1,83±1,06 (ΔNt-LRAT-GFP with OA); -0,68±1,51
983 (LRAT-GFP with ROH); and -1,55±1,08 (ΔNt-LRAT-GFP with ROH) Statistical
984 significance was determined by two-tailed unpaired Student's t-tests, P-values were
985 corrected by the Benjamini-Hochberg procedure **(F)**. Cells were incubated overnight with
986 200 μM OA (red circles) or 20 μM ROH (blue circles) and LD number per cell as a
987 function of total LD volume per cell for LRAT-GFP (closed circles) or
988 ΔNt-LRAT-GFP-expressing (open circles) was analyzed without gating **(G)**. Every data
989 point represents one cell. Lines are moving averages, shades indicate 95% confidence
990 intervals. LRAT-GFP+OA: 35 cells; ΔNt-LRAT-GFP+OA: 79 cells; LRAT-GFP+ROH:
991 43 cells; ΔNt-LRAT-GFP+ROH: 68 cells. * P < 0.05, ** P < 0.01, *** P < 0.001, NS: not
992 significant.
993

994   ***Figure 5.*** *Amphipathic properties of LRAT-Nt and CCT-α P2 helices.*
995   **(A)** Helical wheel projections by HeliQuest of LRAT-Nt (top) and CCT-α P2 (bottom).
996   Colors indicate amino acid categories: hydrophobic (yellow), negatively charged (red),
997   polar (purple), positively charged (blue) and other (gray) residues. The hydrophobic
998   moment is indicated with a black arrow. **(B)** Peptide-membrane interaction energies for
999   LRAT-Nt (top) and CCT-α P2 with pure POPC (red) and with an 85:15 POPC/DOG
1000   mixture (red) over time across DAFT simulation ensembles of 30 simulations each,
1001   showing the region from the 1st to 3rd quartile as shaded areas and the median interaction
1002   energy for each ensemble of simulations as solid line. **(C)** Insertion depth of LRAT-Nt
1003   and CCT-α P2, showing the helical wheels of LRAT-Nt (top) and CCT-α P2 according to
1004   their mean angular orientations, with a red line signifying the position of the helix center,
1005   the thick black line denoting the median position of the lipid head groups across
1006   simulations and the thinner line denoting the standard deviation of the median across
1007   simulations. Colors in the peptides are as described in panel A.
1008
1009   **Figure 6.** *Affinity of LRAT-Nt for retinyl esters in GC-MD.*
1010   **(A)** Binding of LRAT-Nt to lenses consisting of 300 molecules RP (left), 120+180
1011   molecules RP+TOG (middle) and 300 molecules TOG (right). The panels show
1012   preferential binding of the helix (green) to the region of maximal curvature. The RP and
1013   TOG particles are shown in marine and red, respectively. **(B)** Positions of centers of mass
1014   of LRAT-Nt with respect to the membrane as function of the ratio RP:TOG (marine: pure
1015   RP to red: pure TOG). The membrane is shown as density profile, while the positions of
1016   LRAT-Nt are marked with dashed lines. **(C)** Specificity of interaction of LRAT-Nt with
1017   RP over TOG. Each simulation represents a dot and indicates the interaction energy
1018   between LRAT-Nt and RP on the x-axis and between LRAT-Nt and TOG on the y-axis.
1019   Dot size reflects the total number of neutral lipids and the color signifies the ratio
1020   between RP and TOG as indicated. The dashed line has slope -1 and a parallel profile is
1021   indicative of a transition from one pure compound to the other with no preferential
1022   interactions. The observations show a lower interaction with TOG as compared to RP,
1023   resulting in a profile with a reduced slope.
1024
1025   **Figure 7.** *LRAT N-terminal peptide shows strong association with retinyl palmitate*
1026   *droplets.* **(A)** Left, peptide addition to the buffer surrounding a pending oil droplet,
1027   trioleoylglycerol (TOG) or retinyl palmitate (RP), results in a decrease of the interface
1028   surface tension induced by peptide recruitment. **(B)** Related surface tension quantification
1029   over time for TOG and RP oil droplets. Arrows indicate time of LRAT-Nt peptide
1030   injection in the buffer. **(C)** After, equilibrium is reached, the surface of the TOG-droplet
1031   covered by the peptide is compressed, provoking a drop of surface tension. When
1032   compression was stopped, surface tension re-increased, indicating desorption of the
1033   LRAT-Nt peptide from the TOG-buffer interface. Right panel illustrates the manipulations
1034   and consequence on tension and peptide behavior. **(D)** After the LRAT-Nt peptide was
1035   recruited to the RP-droplet surface, the interface was compressed, provoking a surface
1036   tension drop. When compression was stopped, surface tension remained constant,
1037   indicating a strong association of the peptide with the RP-buffer interface. Right panel
1038   illustrates the manipulations and consequence on tension and peptide behavior.

1039
1040
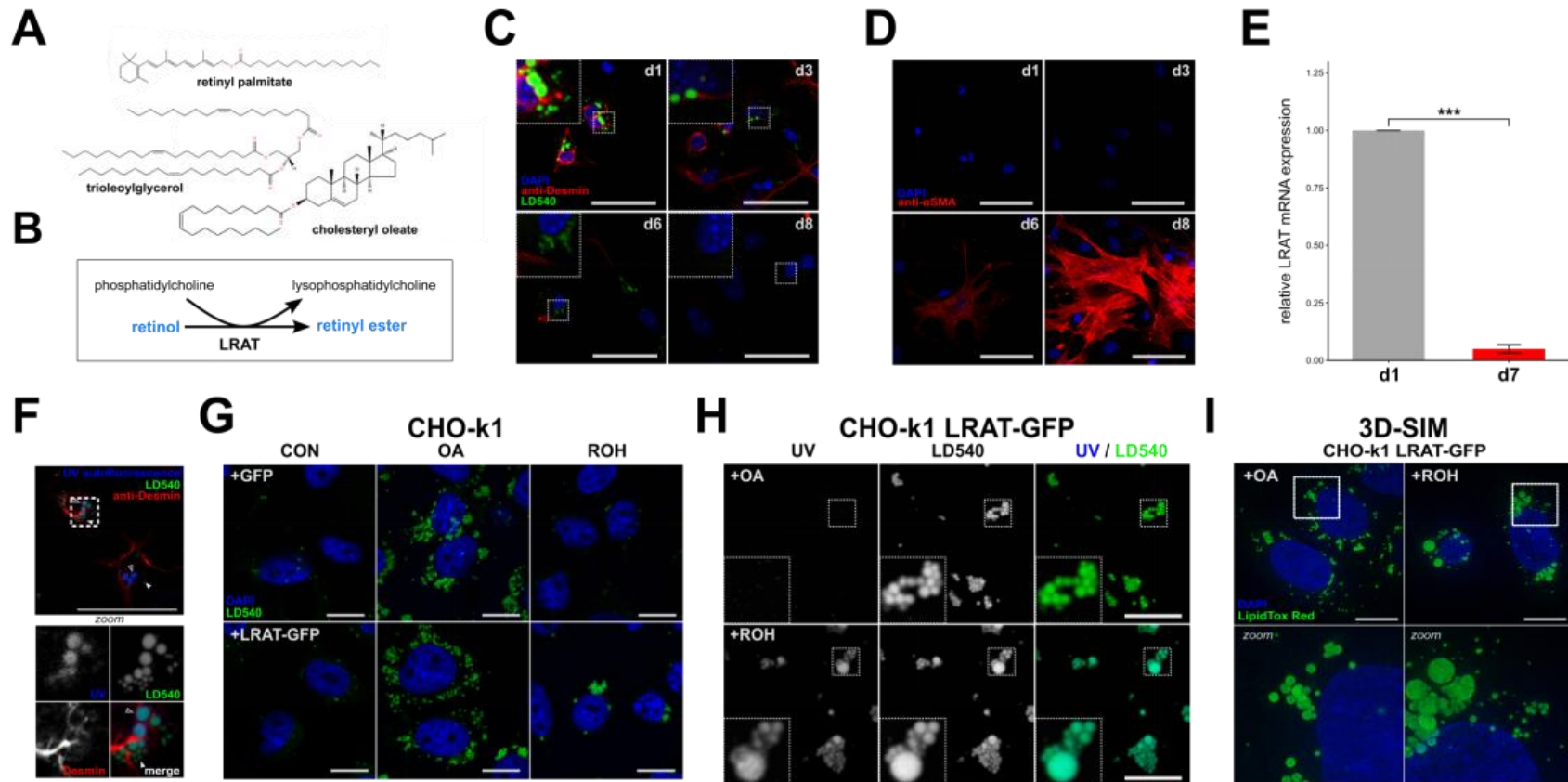
Figures

1043
1044
1045
1046
1047
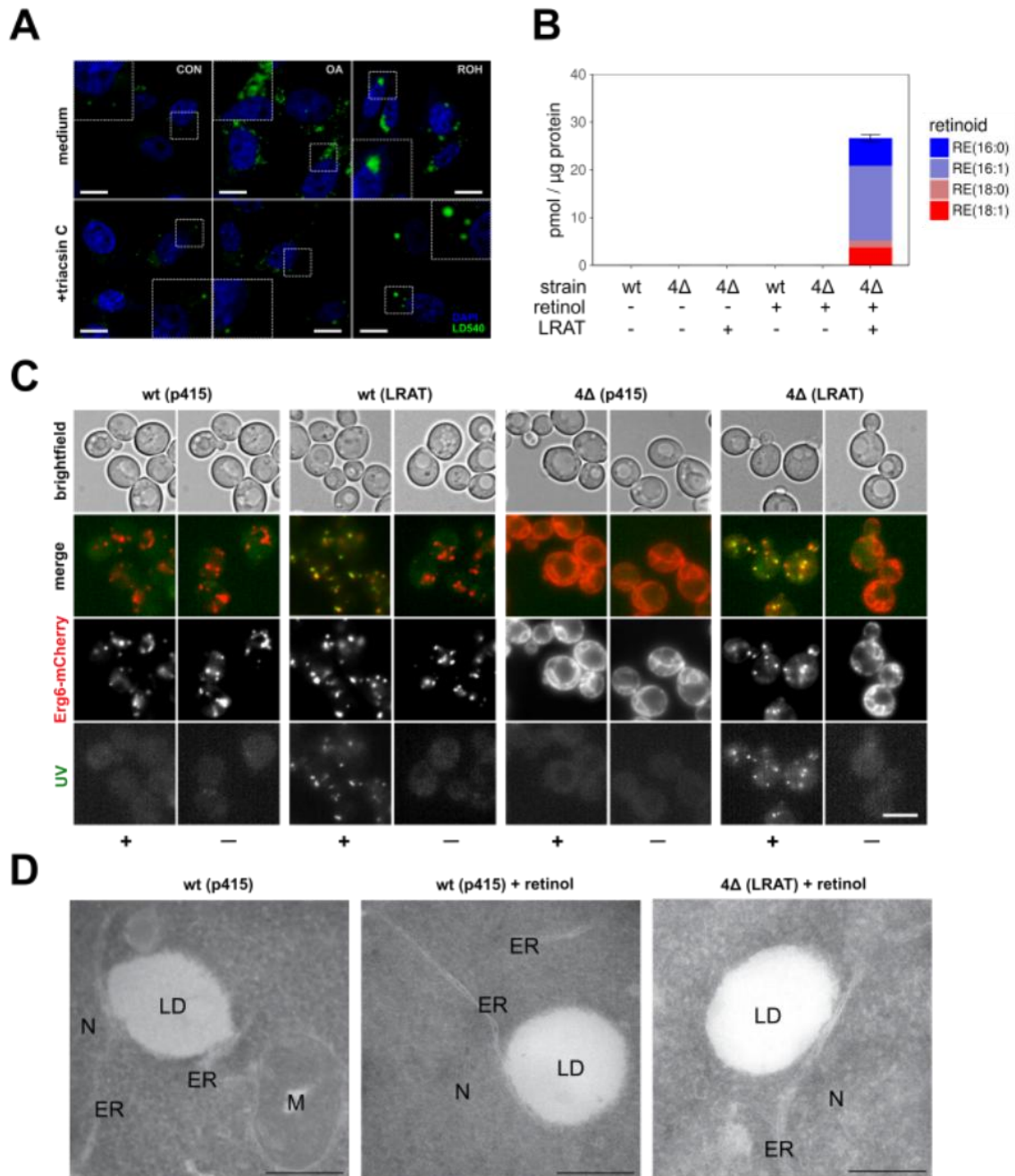1048

Figure 1 Molenaar et al

1049

1050

1051
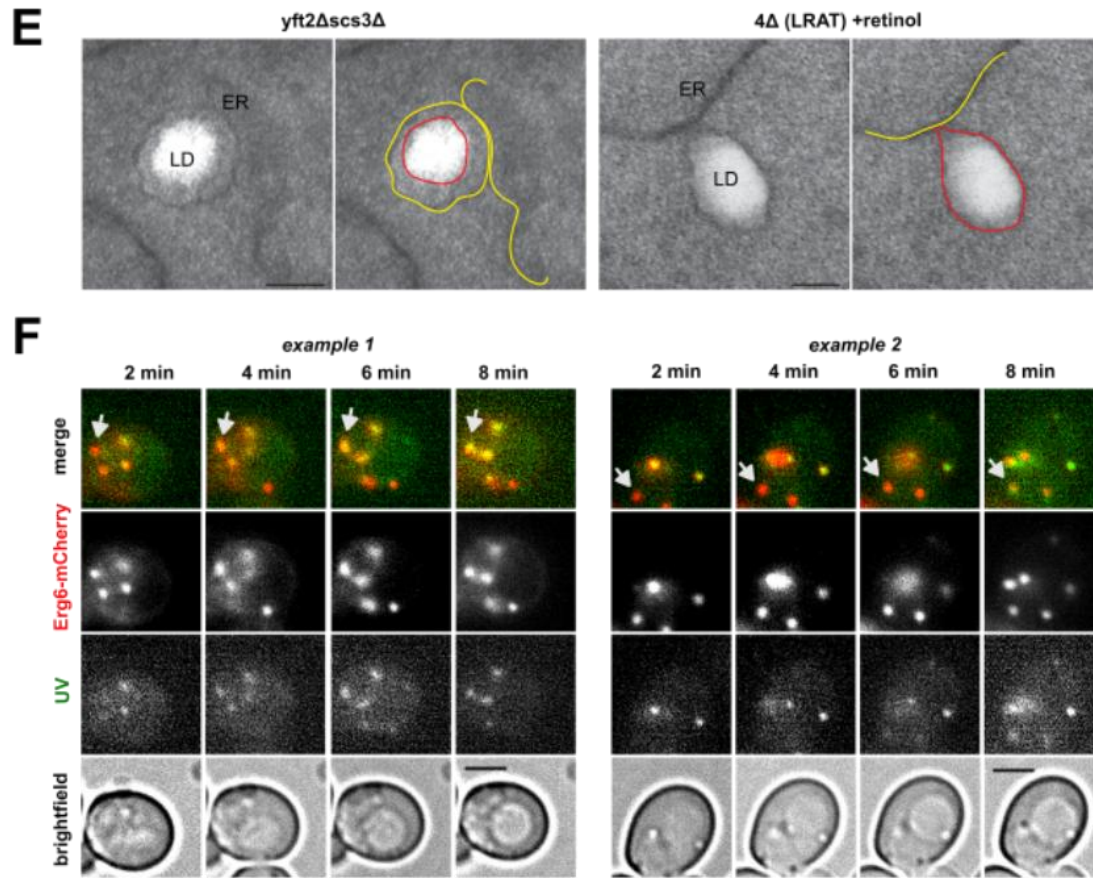
1052

1053

1054 **Figure 2 Molenaar et al**

E

yft2Δscs3Δ

4Δ (LRAT) +retinol

ER

LD

ER

LD

F

example 1

2 min   4 min   6 min   8 min

merge

Erg6-mCherry

UV

brightfield

example 2

2 min   4 min   6 min   8 min

1055

1056

1057

1058

1059

1060

1061

1062

1063

1064

1065

1066

1067

1068   **Figure 2 (*cont.*) Molenaar et al**
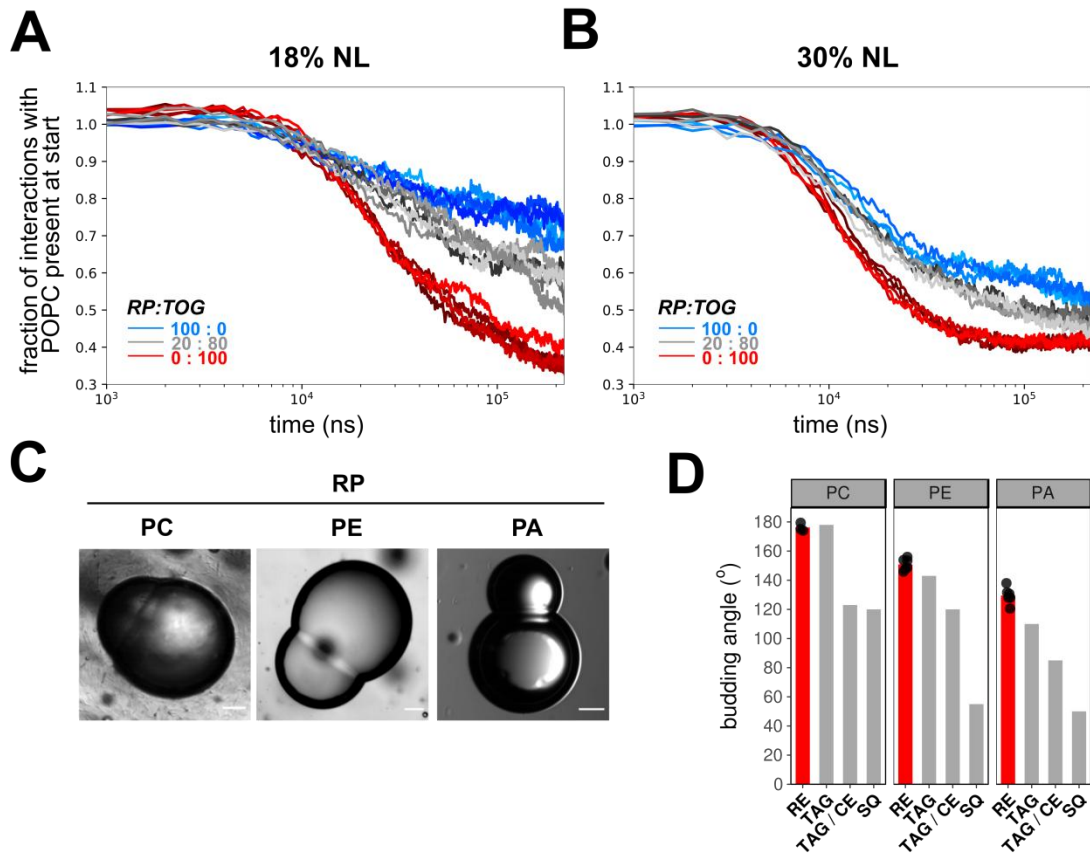
1069

1070

1071
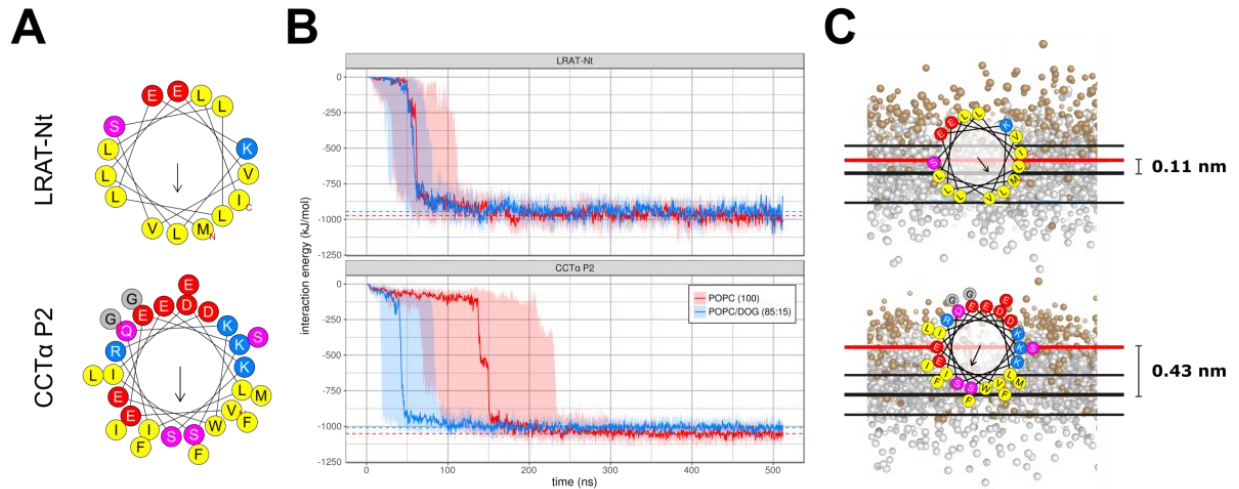
1072

1073

1074

1075

1076

1077

1078

1079

1080

1081

1082 **Figure 3 Molenaar et al**
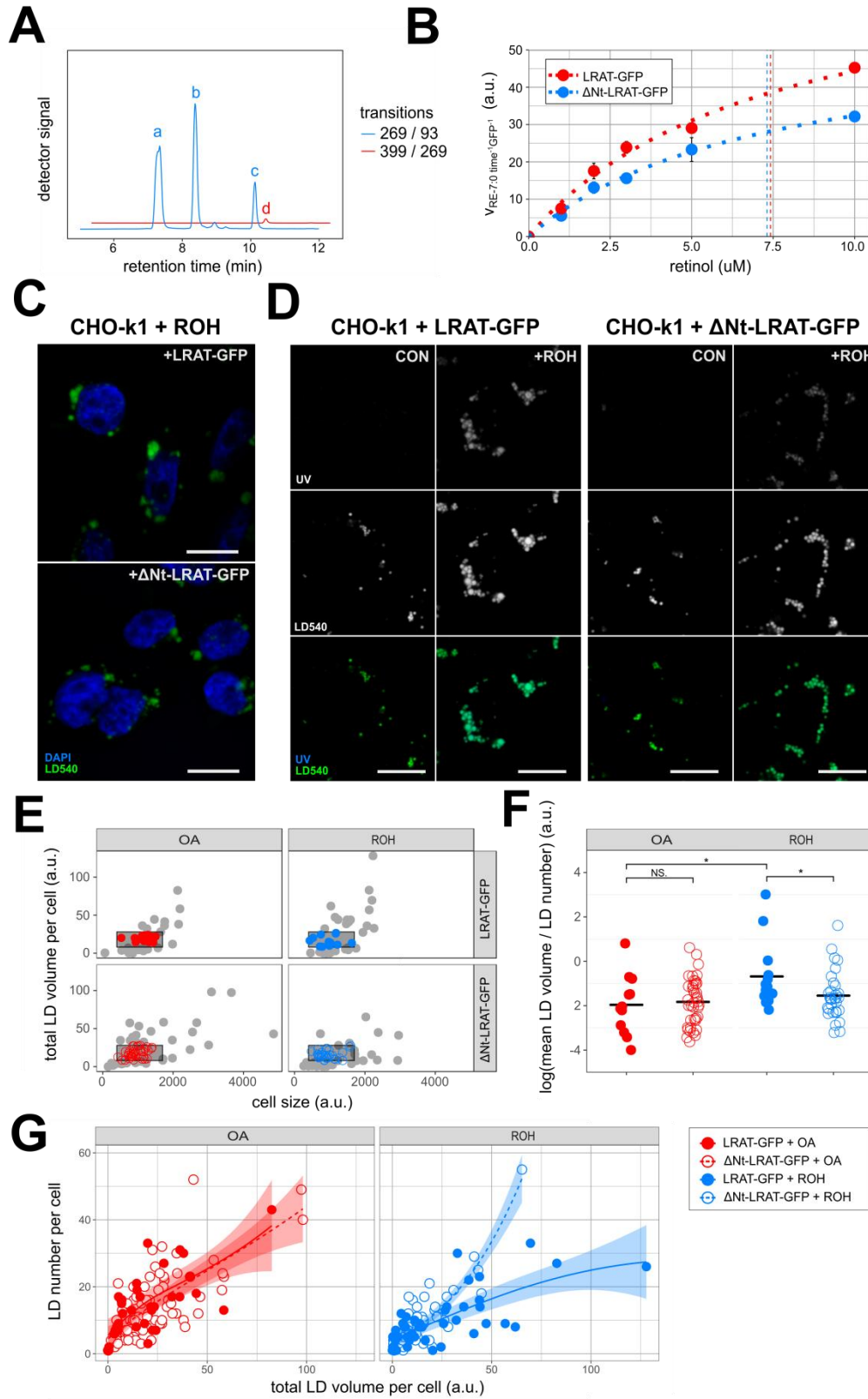
1083

1084 **Figure 4 Molenaar et al**

1085

1086

1087

1088

1089

1090

1091

1092

1093

1094

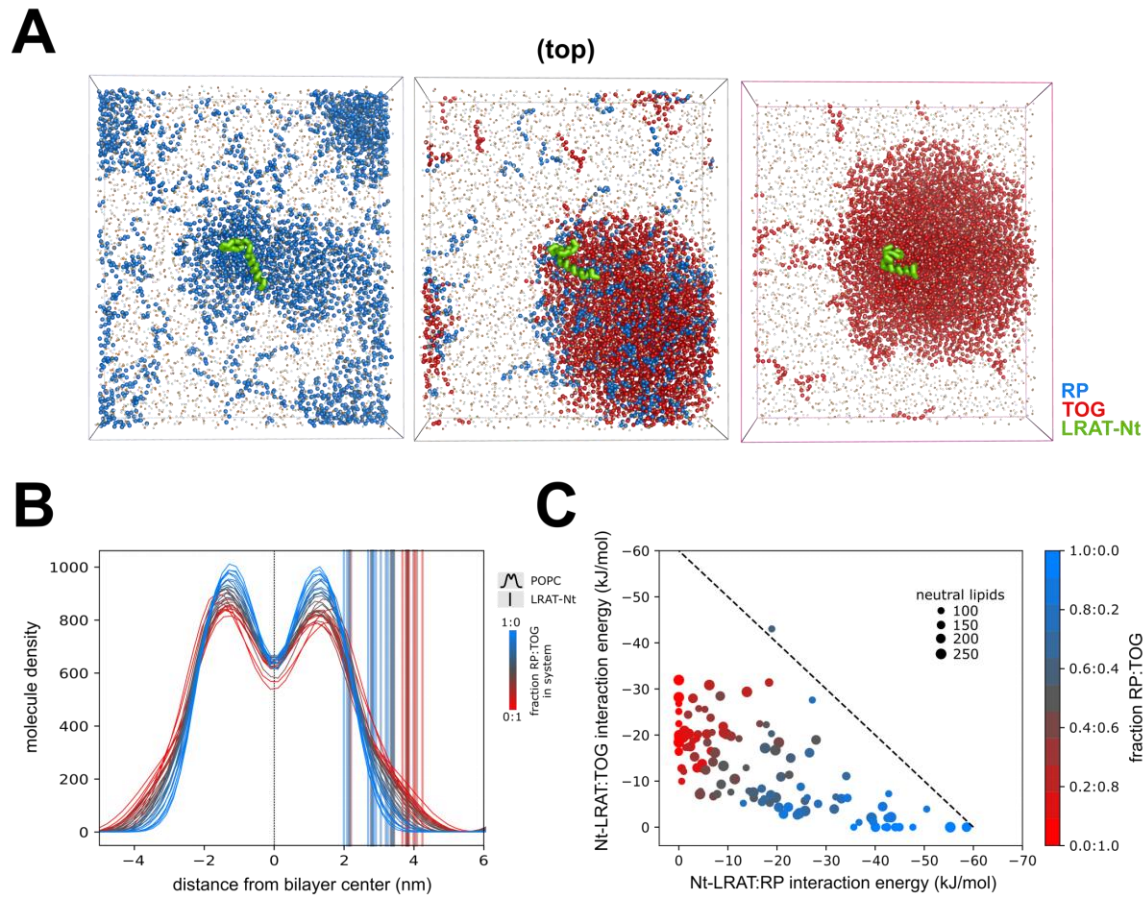1095

1096

1097

1098

1099

1100

1101

1102

1103

1104

1105 **Figure 5 Molenaar et al**

1106

1107

1108
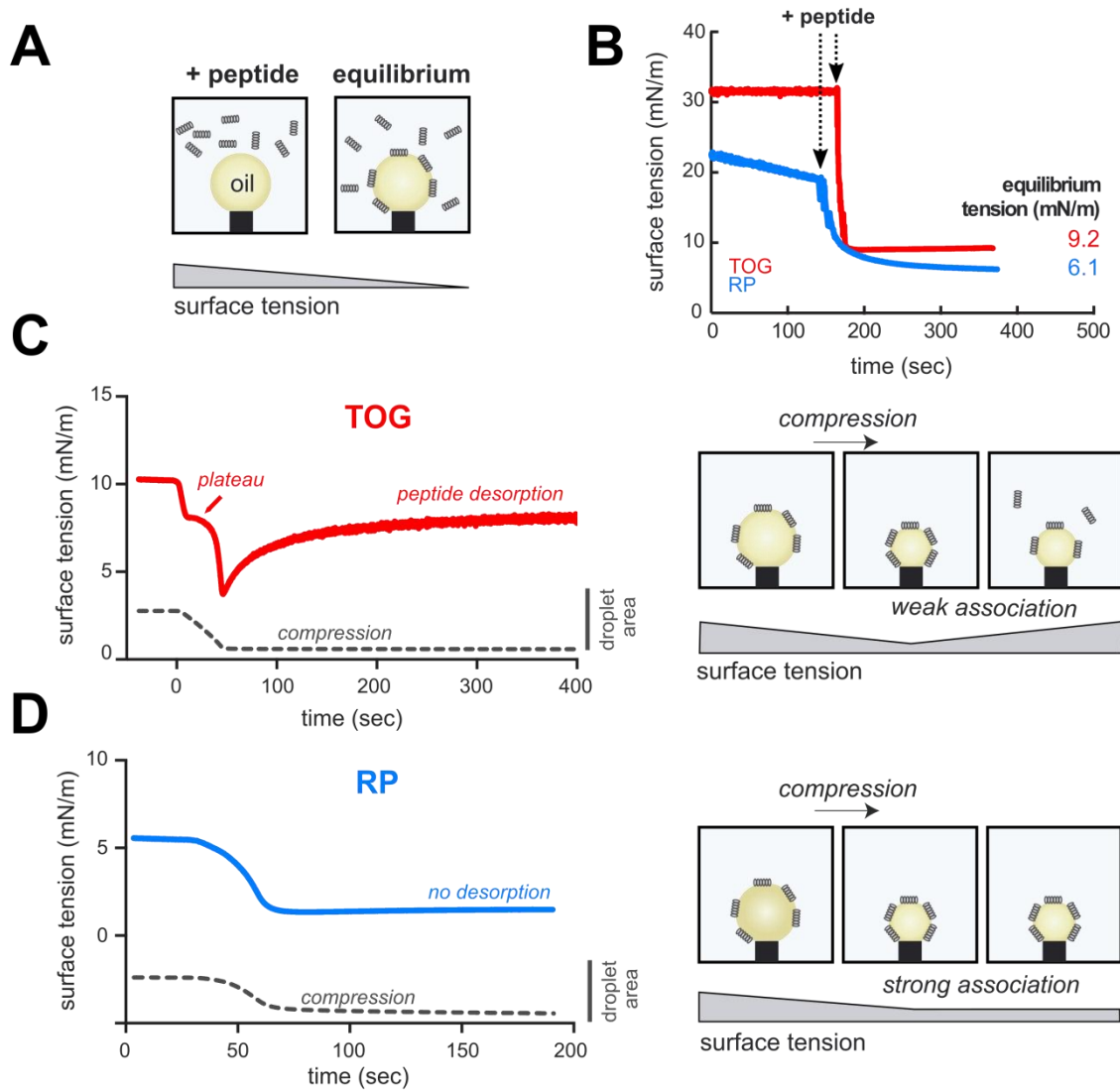
1109

1110

1111

1112

1113

1114

1115

1116

1117

1118

1119 **Figure 6 Molenaar et al**

37

1120

1121

1122

1123

1124

1125

1126

1127

1128

1129 **Figure 7 Molenaar et al**